SIMULATION AND CONTROL STRATEGY DEVELOPMENT OF POWER-SPLIT HYBRID-ELECTRIC VEHICLES

A Thesis
Presented to
The Academic Faculty

by

John P. Arata III

In Partial Fulfillment
of the Requirements for the Degree
Masters of Science in Mechanical Engineering in the
School of Mechanical Engineering

Georgia Institute of Technology
December 2011

SIMULATION AND CONTROL STRATEGY DEVELOPMENT OF POWER-SPLIT HYBRID-ELECTRIC VEHICLES

Approved by:

Dr. Michael Leamy, Co-advisor
School of Mechanical Engineering
Georgia Institute of Technology

Dr. Kenneth Cunefare, Co-advisor
School of Mechanical Engineering
Georgia Institute of Technology

Dr. David Taylor
School of Electrical and Computer Engineering
Georgia Institute of Technology

Date Approved: August 29, 2011

This is dedicated to my family.

ACKNOWLEDGEMENTS

It would be wrong to not give special thanks to my advisor Dr. Michael J. Leamy. Without his patience and dedication, I would not have accomplished the things I have. Dr. Leamy gave me funding, hands-on experience, and an outstanding topic for my thesis while invaluably helping with my development and writing along the way. He motivated me to complete the things I did by continually evolving me as a student. I am very fortunate for every opportunity he has given me - thank you for being the best advisor you could be. I would also like to thank Dr. Kenneth Cunefare for being my co-advisor; providing me with guidance and funding, without which my educational endeavor would not be possible. Lastly, thank you Dr. David Taylor for taking time out of your schedule to serve on my committee and willingness to provide comments and feedback.

Most importantly, I am deeply grateful for my family. My mother deserves special recognition, without her guidance and support (both financial and otherwise) I would not be here. I would also like to especially thank my father, brother, and sister; whether they want to believe it or not they have been fundamental to my success as well.

TABLE OF CONTENTS

LIST OF TABLES

LIST OF FIGURES

LIST OF SYMBOLS

A_f	vehicle frontal area
C_d	drag coefficient
C	cost function
d	cost of changing engine speed
F	force
F_W	force required at driven wheels
g	gravity
G	final-drive ratio
H	angular momentum
H_l	lower heating value of fuel
μ	rolling-resistance coefficient
m	mass
$\dot{m}_f$	fuel flow rate
M	resultant moment
η_B	battery turn-around efficiency
η_{FD}	final-drive efficiency
$\eta_{M/GA}$	*M/GA* efficiency
$\eta_{M/GB}$	*M/GB* efficiency
η_P	planetary gearset efficiency
N	number of teeth on respective gear
φ	smoothing parameter

P_B	battery power
P_e	engine power
P_f	power from burning fuel
$P_{M/GA}$	*M/GA* power
$P_{M/GB}$	*M/GB* power
P_o	transmission output power
P_R	ring gear power
P_S	power sun gear
P_W	wheel power
ρ_{air}	ambient air density
r	respective gear radius
R	planetary gearset characteristic ratio
s	electric power equivalence factor
$\boldsymbol{S_{in}}$	input-state
$\boldsymbol{S_{out}}$	output-state
SR	transmission speed ratio
SR_{mech}	"mechanical point" speed ratio
t	time of drive-cycle
T	end of driving schedule time interval
T_C	carrier gear torque
T_e	engine torque
$T_{M/GA}$	*M/GA* torque
$T_{M/GB}$	*M/GB* torque

T_o	transmission output torque
T_R	ring gear torque
T_S	sun gear torque
V	vehicle velocity
ω_C	carrier gear speed
ω_e	engine speed
$\Delta\omega_{max}$	maximum unpenalized change in engine speed
$\omega_{M/GA}$	*M/GA* rotational speed
$\omega_{M/GB}$	*M/GB* rotational speed
ω_o	transmission output speed
ω_R	ring gear speed
ω_S	sun gear speed

LIST OF ABBREVIATIONS

BLS	backward-looking simulation
BSFC	brake specific fuel consumption
CAFE	Corporate Average Fuel Economy
CL	GM AHS-II clutches 1 through 4
CS	charge sustaining
DOT	Department of Transportation
DP	dynamic programming
EM	electric machine
EPA	Environmental Protection Agency
ESS	energy storage system
EVT	electrically variable transmission
FE	fuel economy
FG	fixed-gear
FLS	forward-looking simulation
FWD	front-wheel drive
GM-AHS II	General Motors Allison Hybrid System II
HEV	hybrid-electric vehicle
IC	internal combustion
M/GA	motor-generator A
M/GB	motor-generator B
MPG	miles per gallon

NVH	noise vibration harshness
OEM	original equipment manufacturer
PID	proportional-integral-derivative
PSD	power-split device
RPM	rotations per minute
RWD	rear-wheel drive
SDP	stochastic dynamic programming
SOC	state-of-charge
SR	speed ratio
THS-II	Toyota Hybrid System II
US	United States

SUMMARY

Power-split hybrid-electric vehicles (HEVs) provide two power paths between the internal combustion (IC) engine and the driven wheels through gearing and electric machines (EMs) composing an electrically variable transmission (EVT). EVTs allow IC engine control such that rotational speed is independent of vehicle speed at all times. By breaking the rigid mechanical connection between the IC engine and the driven wheels, EVTs allow the IC engine to operate in the most efficient region of its characteristic brake specific fuel consumption (BSFC) map. If the most efficient IC engine operating point produces more power than is requested by the driver, the excess IC engine power can be stored in the energy storage system (ESS) and used later. Conversely, if the most efficient IC engine operating point does not meet the power request of the driver, the ESS delivers the difference to the wheels through the EMs. Therefore with an intelligent supervisory control strategy, power-split architectures can advantageously combine traditional series and parallel power paths.

In the first part of this work, two different power-split HEV powertrains are compared using a two-term cost function and steady-state backward-looking simulation (BLS). BLS is used to find battery power management strategies that result in minimized fuel consumption over a user-defined drive-cycle. The supervisory control strategy design approach amounts to an exhaustive search over all kinematically admissible input operating points, leading to a minimized instantaneous cost function. While the approach provides a valuable comparison of two architectures, non-ideal engine speed fluctuations

result. Therefore, in the second part of the work, two approaches for designing control strategies with refined IC engine speed transitions are investigated using high-fidelity forward-looking simulation (FLS). These two approaches include: i) smoothing the two-term cost function optimization results, and ii) introducing a three-term cost function. It is found that both achieve operable engine speed transitions, and result in fuel economy (FE) estimates which compare well to previous BLS results. It is further found that the three-term cost function finds more efficient operating points than the smoothed two-term cost function approach. From the investigations carried out in parts one and two of this work, a two-phase control strategy development process is suggested where control strategies are generated using efficient steady-state BLS models, and then further tested and verified in high-fidelity FLS models. In conclusion, the FLS results justify the efficacy of the two-phased process, suggesting rapid and effective development of implementable power-split HEV supervisory control strategies.

CHAPTER 1

INTRODUCTION

Due to a finite crude oil supply and increased demand, fuel efficient vehicle propulsion is a topic of interest. Figure 1.1 provides the time-history of the Unites States (US) crude price of oil from 1998 to the present. The crude price of oil per barrel has increased 1370% from $8.51 in December of 1998 to $116.53 in April of 2011 [1]. The US Government has placed tight fuel economy (FE) standards on cars and light trucks with the goal of reducing oil consumption. Corporate Average Fuel Economy (CAFE) legislation was passed by Congress in 1975 and requires vehicle manufacturers to comply with FE standards set by the Department of Transportation (DOT) [2]. In July 2011, the US government announced that in 2025 CAFE standards will require vehicle original equipment manufacturers (OEMs) to average 54.5 miles per gallon (MPG) across their entire fleet [3]. To discourage the purchase and production of fuel inefficient vehicles, the Gas Guzzler Tax is also being imposed on new vehicles [4].

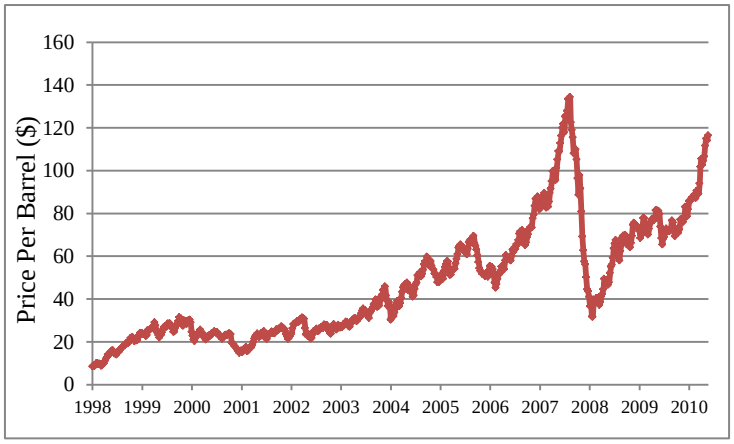

Figure 1.1: Average US oil price has increased 1370% since December 1998 [1].

The Environmental Protection Agency (EPA) was formed in 1970 to ensure that all Americans are protected from health and environmental risks [5]. One of the numerous ways the EPA protects the environment is by policing the tailpipe emissions of vehicles. The Tier 2 Vehicle and Gasoline Sulfur program is part of initiatives that will reduce emissions from passenger vehicles, highway trucks and buses, and non-road diesel equipment [6]. The Tier 2 regulations affect every new passenger vehicle and every gallon of gasoline sold in the US to encourage cleaner vehicles. Resulting from heightened FE regulations and emissions standards, OEMs are presented with increased design challenges. With the current status of limited all-electric and hydrogen infrastructures, charge sustaining (CS) hybrid-electric vehicles (HEVs) show potential for increasing FE and reducing emissions in the short-term.

1.1 Hybrid-Electric Vehicle Background

The adjective hybrid refers to something that "has different types of components performing essentially the same function" [7]. In the context of HEVs, hybrid implies the blend of conventional ignition-based propulsion and electric propulsion. Internal combustion (IC) engine operation is best suited for steady power delivery (e.g., highway driving at constant cruising speed), as opposed to dynamic power delivery (e.g., urban or variable speed driving). For dynamic power delivery over a large range of vehicle speeds, conventionally propelled vehicles and their transmissions are constrained by a finite number of fixed-gear (FG) ratios that can result in potentially inefficient engine operation. The operation of the IC engine and electric machines (EMs) in architectures ultimately dictate the powertrain's efficiency. Since IC engines are more variable in their

efficiency than EMs, it suffices to consider the IC engine operation when qualitatively assessing overall powertrain efficiency. To achieve increased efficiencies, three fundamental HEV architectures are in use today: series, parallel, and power-split. The characteristics of each architecture are defined in the sections to follow.

1.1.1 Series Hybrid-Electric Vehicle

A series HEV configuration is shown in Figure 1.2. Series architectures allow the IC engine to operate independently of the road-load conditions as the IC engine is not directly connected to the driven wheels. By breaking the rigid connection between the IC engine and driven wheels, the IC engine can provide steady highly-efficient operation. The tractive motor consumes energy from the IC driven generator or the energy storage system (ESS). Since not rigidly connected to the driven wheels, the IC engine is operated near its optimal efficiency throughout operation. Excess delivered IC engine power is stored in the ESS and used advantageously in the future. Series electro-mechanical power delivery is best suited for urban driving with significant vehicle speed fluctuations. However, electro-mechanical power delivery is less efficient than purely mechanical paths due to energy conversion losses.

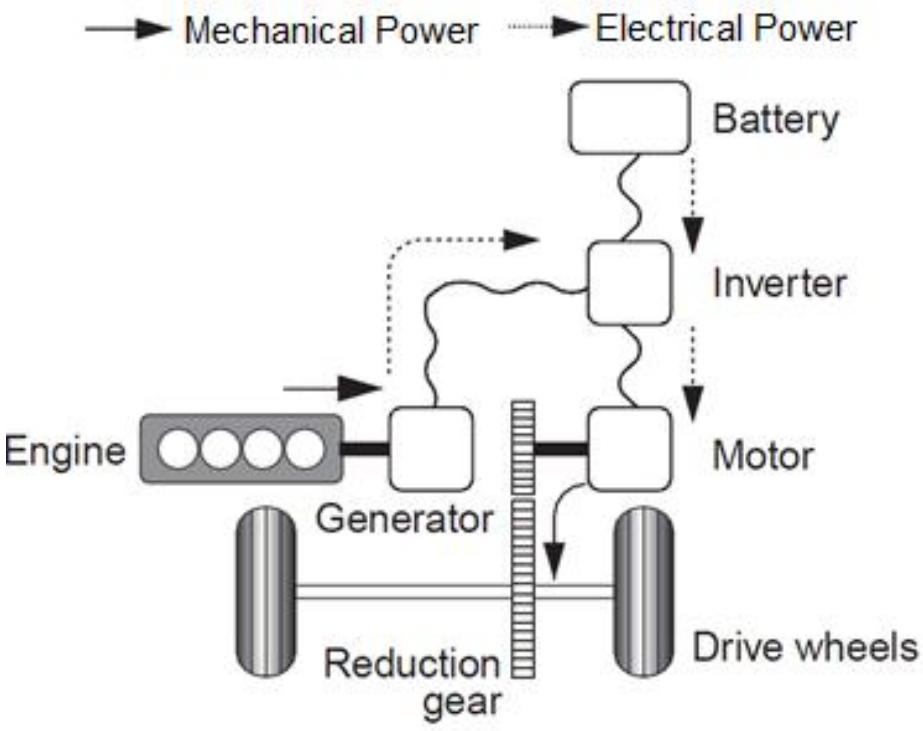

Figure 1.2: Series HEV architecture, reproduced from [8]

1.1.2 Parallel Hybrid-Electric Vehicle

A parallel HEV configuration is shown in Figure 1.3. Parallel architectures enable two power paths between the power plant and the driven wheels: 1) a highly-efficient mechanical path to transmit input IC engine power, and 2) an electro-mechanical path powered by the ESS. The electro-mechanical path captures regenerative braking and supplements the IC engine in order to reach higher efficiencies by delivering a portion of the road-load requirements. However, engine speed and efficiency is still constrained by a finite number of FG ratios.

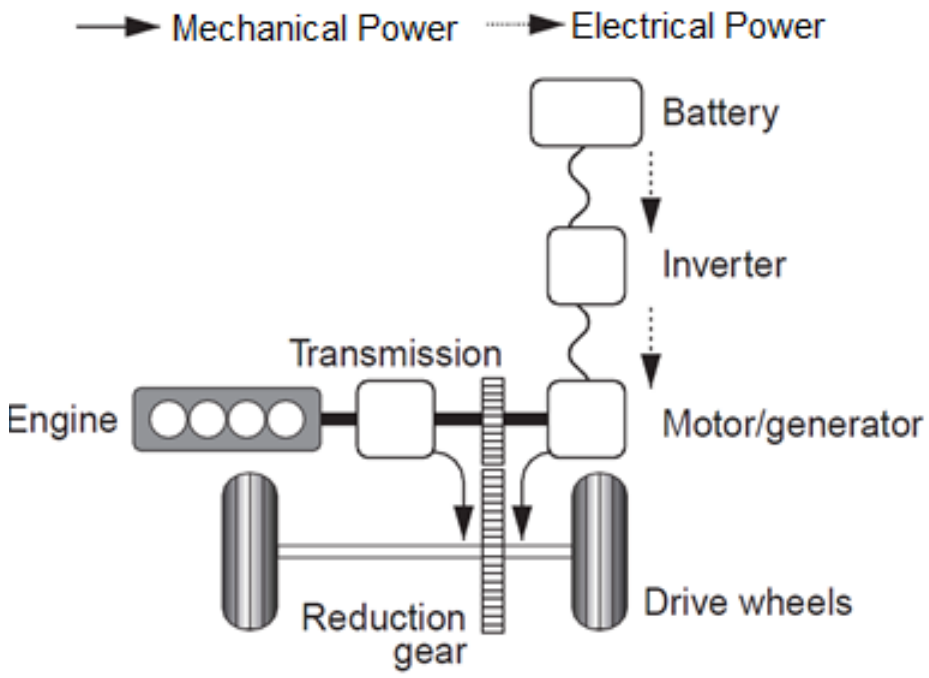

Figure 1.3: Parallel HEV architecture, reproduced from [8]

1.1.3 Power-Split Hybrid-Electric Vehicle

A power-split HEV configuration is shown in Figure 1.4. Power-split HEV designs provide two power paths between the IC engine and the driven wheels through gearing and EMs using an electrically variable transmission (EVT). EVTs allow IC engine control such that rotational speed is independent of vehicle speed, a supervisory control strategy degree of freedom. The addition of an on-board ESS, in HEVs a high voltage electric energy buffer, and EMs also allow IC engine power to be chosen independently of wheel power. By breaking the rigid mechanical connection between the IC engine and the driven wheels, EVTs allow the IC engine to operate in the most efficient region of its characteristic BSFC map. If the most efficient IC engine operating point produces more power than is requested by the driver, the excess IC engine power can be stored in the

ESS and advantageously used in the future. Conversely, if the most efficient IC engine operating point does not meet the power request of the driver, the EMs powered by the ESS deliver the difference to the wheels. Therefore with an intelligent supervisory control strategy, power-split architectures can advantageously combine series and parallel power paths between the vehicle's power-plants and driven wheels.

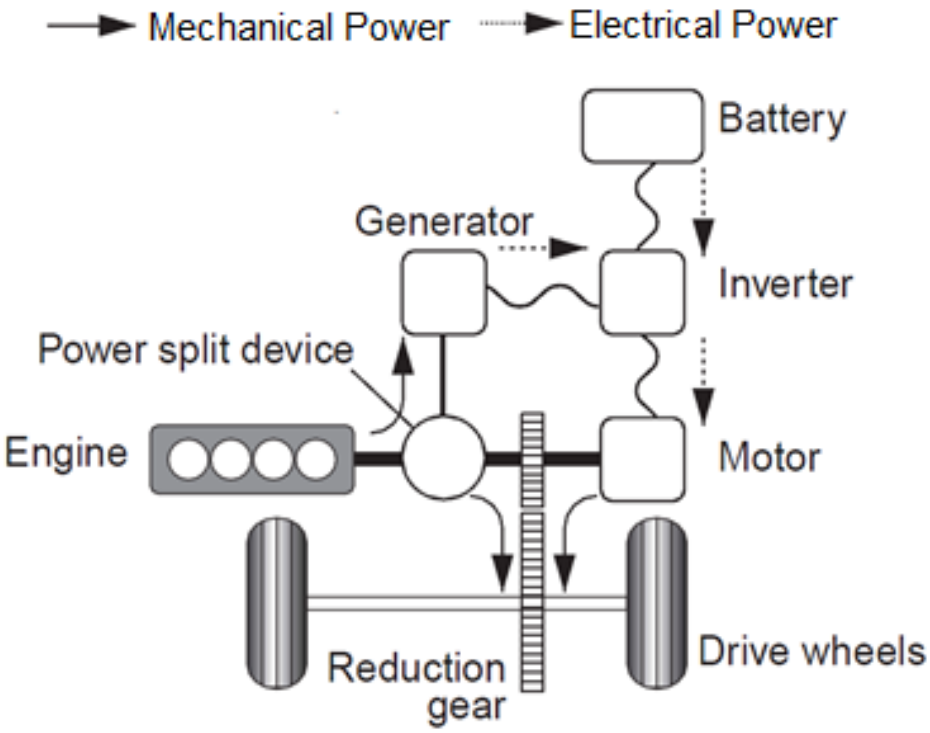

Figure 1.4: Power-Split HEV architecture, reproduced from [8]

1.2 Literature Review

Since their introduction in the early 1970's [9], EVTs have evolved into two distinct configurations commonly used today: namely the one-mode and the two-mode EVT. The historical development of power-split transmissions and a trace of their evolution can be found in [10]. One-mode EVTs have been extensively studied, specifically as they

pertain to the Toyota Hybrid System II (THS-II) input-split hybrid powertrain system. Detailed descriptions of their basic operation can be found in [11, 12]. It has also been shown that two-mode power-split transmissions show improvements in efficiency and dynamic performances in comparison to one-mode planetary transmissions [13-16].

Due to energy conversion losses in the electrical energy path, engine operation on the engine optimal operation line may not minimize fuel consumption in power-split hybrids. Other studies have quantified transmission efficiency, and in doing so, have shown that a critical value of a speed ratio can be defined which determines the onset of power circulation loops [17]. By considering transmission losses and engine specific fuel consumption, system operating points minimizing fuel consumption can be found [18]. As detailed next, a number of time-horizon *dependent* and *independent* optimization approaches have been applied to the supervisory control strategy design of power-split HEVs [19].

1.2.1 Time Horizon Dependent Methods

Time-horizon *dependent* optimization methods enable comparing HEV architectures' theoretical maximum efficiencies by assuming *a priori* knowledge of the drive-cycle. Dynamic Programming (DP) finds the globally optimum solution by optimizing numerically with respect to a specific drive-cycle (e.g., DP results can be sub-optimal for another drive-cycle) [20-22]. Pontryagin's Minimum Principle and Pareto Optimization have also been applied to the HEV supervisory control strategy design challenge [23- 25], providing an analytical formulation that also considers the entire driving cycle. Stochastic dynamic programming (SDP) does not optimize solutions for a specific drive-

cycle, but for assumed road-load conditions with known probabilities [26, 27]. SDP results can be sub-optimal or charge depleting when applied to a driving schedule with drastically different road-load conditions than those assumed. Time-horizon *dependent* routines optimize a cost function over an entire driving schedule and are therefore not implementable without user input at the inconvenience of the consumer.

1.2.2 Time Horizon Independent Methods

Time-horizon *independent* optimization routines have also been used to design HEV supervisory control strategies. Heuristic rule-based methods and fuzzy logic with optimized thresholds and transitions have been employed to address this design problem [28, 29]. The instantaneous minimization of cost functions has also been used to find the most efficient split between on-board energy sources. By translating electric power into an equivalent energy consumption term of the cost function, total consumption can be minimized [30]. Instantaneous equivalent minimization strategies have been shown to be close to the optimal DP results and good candidates for developing implementable control algorithms but lead to varied engine power commands [31].

1.3 Outline

This section will summarize the material to be presented in this work. Chapter 1 has motivated a need for environmentally friendly vehicle propulsion. HEVs show promise for filling that void in the near future; the three HEV architectures commonly used today are defined in Chapter 1. This thesis studies the supervisory control strategy development of power-split HEVs. In Chapter 2, two different power-split HEV powertrains are compared using a two-term cost function and steady-state backward-looking simulation (BLS). While valuable for comparing the studied architectures, it is

found that these results idealistically vary IC engine speed. Chapter 3 of this work presents two approaches for designing control strategies with refined IC engine speed transitions. These two methods include: 1) smoothing the two-term cost function optimization results, and 2) introducing a three-term cost function. The results of these two methods are then tested and verified in high-fidelity forward-looking simulation (FLS). It is found that both achieve operable engine speed transitions, and result in fuel economy estimates which compare well to previous BLS results. This suggests a two-phase control strategy development process where control strategies are generated using efficient steady-state backward-looking models, and then further tested and verified in high-fidelity forward-looking models. Close comparisons are documented for component operation dictated by the BLS-derived control strategy with that computed using FLS. This justifies the efficacy of the two-phased process, suggesting rapid and effective development of implementable power-split HEV supervisory control strategies. Lastly, Chapter 4 summarizes the work in this thesis.

1.4 Contributions

This thesis contributes the following:

- A steady-state comparison between one-mode and two-mode power-split architectures
- Addresses rapid engine speed transients resulting from steady-state models with two refinement techniques
- Develops a dynamic one-mode power-split HEV model to test and verify supervisory control strategies

- Introduces an efficient two-phase development process for designing implementable supervisory control strategies

This work has also led to the following publications:

1. Arata, J., Leamy, M., Meisel, J., Cunefare, K., Taylor, D., 2011, "Backward-Looking Simulation of the Toyota Prius and General Motors Two-Mode Power-Split HEV Powertrains," *SAE International Journal of Engines,* Vol. 120 (in press).
2. Arata, J., Leamy, M., Cunefare, K., "Power-Split HEV Control Strategy Development with Refined Engine Transients," *submitted,* Proceedings of the 2012 SAE World Congress.

CHAPTER 2

STEADY-STATE POWER-SPLIT HEV CONTROL STRATEGY DEVELOPMENT

This chapter presents a comparative analysis of two different power-split HEV powertrains using BLS. Compared are the front-wheel drive (FWD) THS-II and the FWD General Motors Allison Hybrid System II (GM AHS-II). Although previous publications evaluate the rear-wheel drive (RWD) GM AHS-II powertrain, this work presents an analysis of the FWD version. The Toyota system employs a one-mode EVT, while the GM system employs a two-mode EVT. Both powertrains are modeled with the same assumed mid-size sedan chassis parameters. Each design employs their native IC engine because the transmission's characteristic ratios are designed for the respective engine brake specific fuel consumption (BSFC) maps. Due to the similarities (*e.g.*, power, torque, displacement, and thermal efficiency) between the two IC engines, the fuel consumption and performance differences of the native engines are neglected in this comparison. The road-load parameters defining each system are used to calculate the required mechanical power at the driven wheels necessary to follow a given drive-cycle. Admissible engine operating states are sought based on component performance limitations and the required mechanical power at the driven wheels. Each IC engine operating point defines an accompanying battery power consistent with the constraints of the electric machines. The design approach is to exhaustively search all admissible states and minimize an instantaneous cost function based on engine power and battery power, at each time instant of the drive-cycle. Two cost functions are considered which weight

battery power usage using either a linear, or an inverse-tangent, function of the current battery state-of-charge (SOC). Selected operational states are then compared against each other based on the flexibility and power delivery capabilities of the powertrains. Fuel minimizing cost functions are determined with the assistance of a charge sustaining index introduced by this paper. Finally, the most fuel efficient choices are used to determine the expected efficiency of both powertrains considered.

2.1 Toyota Hybrid System II

The THS-II architecture is an input-split EVT whereby the input engine power is effectively split between a mechanical and electro-mechanical path. The THS-II powertrain is composed of several key components: battery, IC engine, two inverters, two motor-generator EM (*M/GA* and *M/GB*), and a planetary power-split device (PSD). Figure 2.1 displays the FWD THS-II powertrain along with the positive power conventions assumed throughout this work.

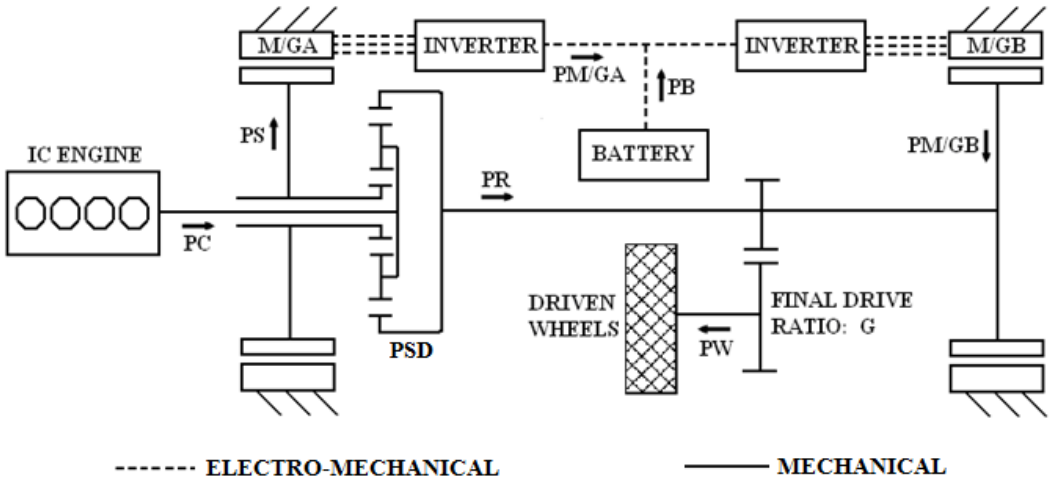

Figure 2.1: Cut-away of the THS-II powertrain

Diversion of IC engine power into the electro-mechanical power path is enabled by the PSD. The PSD allows IC engine power to be simultaneously transferred to *M/GA* and the wheels. The carrier shaft of the PSD is directly linked to the engine and mechanically transmits the motive engine power to the outer ring gear and inner sun gear via pinion gears. EM *M/GA* typically generates electricity and is connected to the sun gear, giving rise to the serial power path. The ring gear is directly coupled to the larger propulsive EM *M/GB* and the front axle through fixed reduction gearing, giving rise to the parallel path. The smaller *M/GA* is controlled such that the machine is capable of imposing the speed ratio (SR), the ratio of input engine speed to output ring gear speed, through the transmission using the PSD sun gear [15]. The larger *M/GB* does not affect the speed ratio as it is connected directly to the wheels. The rotational speed of the common *M/GB*-output shaft $\omega_{M/GB} = \omega_o$ is proportional to vehicle speed by final-drive ratio *G*. Thus for any prescribed vehicle speed, transmission output angular velocity ω_o is known. Both EMs are capable of bi-directional energy flow by operating as either a motor or as a generator; however *M/GA* converts electric power into mechanical power when it is spinning in the negative direction or it is boosting engine speed [25]. The battery is an energy buffer that cannot be externally recharged, therefore battery SOC must be maintained within usable limits or the integrity of the battery is jeopardized. Diversion of engine power into the electro-mechanical power path in Figure 2.1 is enabled by the PSD and will be detailed next.

The PSD allows the IC engine power to be simultaneously transferred to *M/GA* and the wheels. A three axis simple planetary gearset with three pinion gears is the PSD in the THS-II system and is shown in Figure 2.2.

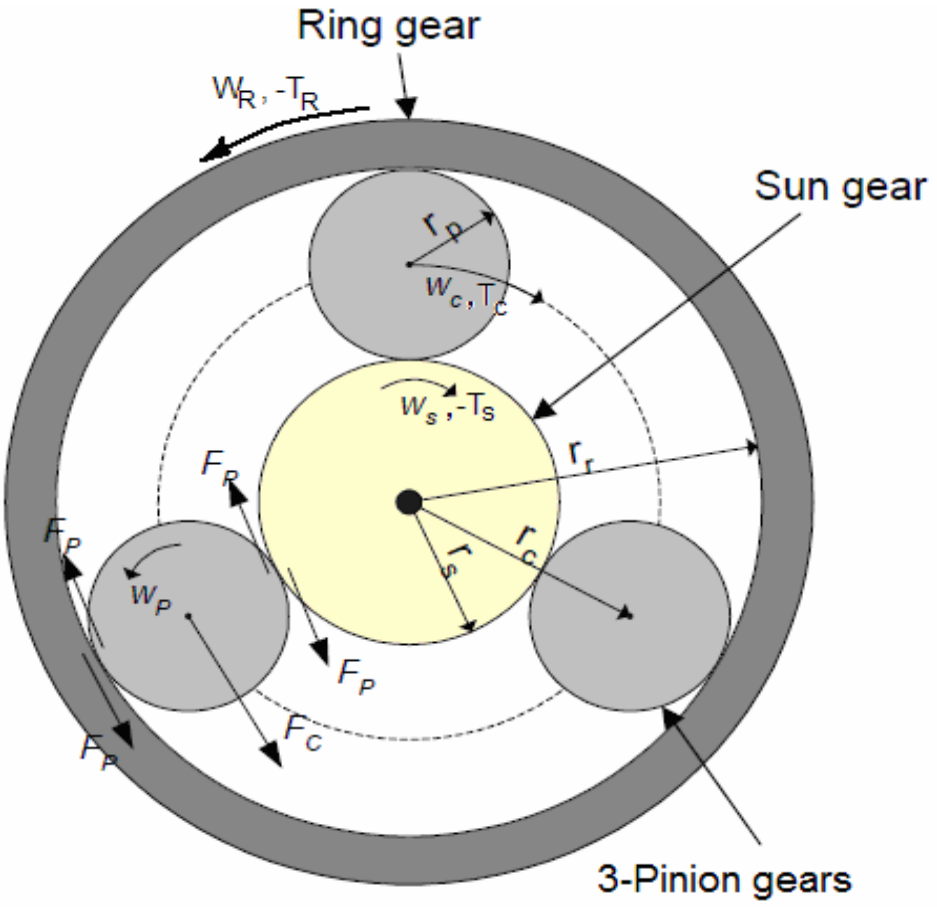

Figure 2.2: A simple planetary gearset is the PSD in the THS-II powertrain, reproduced from [32].

The characteristic ratio for the planetary gearset *R* is defined as,

$$R = \frac{r_{sun}}{r_{ring}} = \frac{N_{sun}}{N_{ring}}, \tag{2.1}$$

where r is the radius and N is the number of teeth on the respective gears. Torque constraints on the simple planetary are derived by imposing a power balance neglecting gearset accelerations and losses, reducing to the steady-state torque relationship,

$$T_C = (1 + R)T_R = \frac{1+R}{R} T_S \,, \tag{2.2}$$

where T_C, T_R, and T_S are the carrier, ring, and sun gear torques respectively. Kinematic speed constraints based on equal speeds at points of contact where meshing occurs,

$$(1 + R)\omega_C - \omega_R - R\omega_S = 0, \tag{2.3}$$

exist such that ω_C, ω_R, and ω_S are the carrier, ring, and sun gear rotational velocities respectively. From Equation (2.2) and Equation (2.3), it can be noted there are two independent speeds and one independent torque constraining the power delivery through all branches of the THS-II PSD. In what follows, this work returns to using torques T_e and $T_{M/GA}$ for T_C and T_S, respectively, where T_e denotes IC engine torque and $T_{M/GA}$ denotes *M/GA* torque. Similarly, angular velocities ω_e, ω_o, and $\omega_{M/GA}$ will be used to represent ω_C, ω_R, and ω_S, respectively, where ω_e denotes the IC engine angular velocity and $\omega_{M/GA}$ denotes the angular velocity of EM *M/GA*. The kinematic torque and speed constraints of the THS-II PSD can therefore be expressed as,

$$T_e = (1 + R)T_R = \frac{1+R}{R} T_{M/GA}, \tag{2.4}$$

$$(1 + R)\omega_e - \omega_o - R\omega_{M/GA} = 0. \tag{2.5}$$

Two relevant facts regarding planetary gearsets are: 1) when any two terminals are connected together, all three terminals rotate at the same speed in the same direction, *i.e.*, the gearset becomes locked-up, and 2) when any terminal is stationary, no power flows through that terminal, *i.e.*, the gearset reduces to a conventional two-terminal gearset.

The transmission speed ratio,

$$SR = \frac{\omega_e}{\omega_o} = \frac{1}{1+R} + \frac{R}{1+R}\frac{\omega_{M/GA}}{\omega_o}, \tag{2.6}$$

is an important measure that dictates the direction of power flow through *M/GA* by changing the rotational direction of the sun gear and ultimately the machine's functionality, motoring versus generating. Operation where the transmission is rotating but *M/GA* is stationary occurs at the "mechanical point" speed ratio where all of the input engine power is mechanically delivered to the common ring gear-*M/GB* output shaft. The "mechanical point" tends to be the most efficient speed ratio for power flow through the transmission since none of the transmitted mechanical power is subject to *M/GA* energy conversion losses. The "mechanical point" speed ratio is then,

$$SR_{mech} = \frac{1}{1+R}. \tag{2.7}$$

The smaller *M/GA* is controlled such that the machine is capable of controlling the speed ratio through the transmission using the sun gear, while the larger *M/GB* does not affect the speed ratio as it is connected directly to the wheels.

Power flow through each branch of the PSD is modeled with component efficiencies and constraining speed and torque equations. The IC engine is characterized by its thermal efficiency and both EMs are characterized by their efficiency maps, inverter energy conversion losses included. The required wheel power,

$$P_W = \eta_{FD}[P_R + P_{M/GB}], \tag{2.8}$$

is delivered from a combination of output ring gear power P_R and *M/GB* propulsive power $P_{M/GB}$ through the final-drive gearing as shown in Figure 2.1. In Equation (2.8), P_W is the mechanical power delivered to the wheels and η_{FD} is the

efficiency of the final-drive gearing. For the final-drive gearing, a constant efficiency 0.95 will be used in this analysis since the efficiency is known to be nearly independent of the road-load conditions [33]. The direction and type of power, either generating or motoring, delivered by *M/GB* depends on the direction of the applied torque T_o. The output ring gear power is mechanically transmitted through the planetary gearset. From the conservation of power, the output ring gear power is,

$$P_R = \eta_P[P_e - P_{M/GA}], \tag{2.9}$$

where P_e is the input engine power into the carrier gear, $P_{M/GA}$ is the power delivered to *M/GA*, and η_P is the planetary gear efficiency in transferring engine power through the planetary gearset. For the planetary gearset, a constant efficiency of 0.98 will be used in this analysis because the efficiency is known to be nearly independent of the road-load conditions [33]. The IC engine is continuously connected to the carrier gear $T_e = T_C$, therefore from Equation (2.4), the output ring gear torque and torque delivered to *M/GA* with losses are,

$$T_R = \eta_P \frac{1}{1+R} T_e, \tag{2.10}$$

$$T_{M/GA} = \eta_P \frac{R}{1+R} T_e, \tag{2.11}$$

where η_P reduces the torque delivered by the engine. The ring and sun gear output powers are,

$$P_R = \eta_P \frac{1}{1+R} T_e \omega_o, \tag{2.12}$$

$$P_{M/GA} = \eta_P \frac{R}{1+R} T_e \omega_{M/GA}, \tag{2.13}$$

where the rotational speed of *M/GA* on the sun gear can by calculated using Equation (2.5) or the definition of the transmission speed ratio in Equation (2.6),

$$\omega_{M/GA} = \frac{(1+R)\omega_e - \omega_o}{R} = \frac{1+R-1/SR}{R}\omega_e. \tag{2.14}$$

Battery power is dependent on the functionality of *M/GA* and *M/GB*. Throughout this analysis the positive battery power convention is out of the battery and battery turn-around losses are neglected; *i.e.* $\eta_B = 1$. This has no bearing on the comparison of the two architectures considered herein. When rotating in the positive direction, *M/GA* acts as a generator by absorbing mechanical power through the sun gear and converting it into electrical power before final transmission to the electrical bus. For $SR > SR_{mech}$, battery power,

$$P_B = \begin{cases} \frac{T_{M/GB}\omega_o}{\eta_{M/GB}} - \eta_{M/GA}\eta_P \frac{R}{1+R} T_e \omega_{M/GA} & T_{M/GB} > 0 \\ \eta_{M/GB} T_{M/GB}\omega_o - \eta_{M/GA}\eta_P \frac{R}{1+R} T_e \omega_{M/GA} & T_{M/GB} < 0 \end{cases}, \tag{2.15}$$

depends on *M/GB* functionality. When rotating in the negative direction, *M/GA* acts as a motor by consuming battery power and converting it into mechanical power, delivering it to the PSD and assisting in propelling the vehicle. The ensuing battery power for $SR < SR_{mech}$ operation,

$$P_B = \begin{cases} \frac{T_{M/GB}\omega_o}{\eta_{M/GB}} - \frac{\frac{R}{1+R} T_e \omega_{M/GA}}{\eta_{M/GA}} & T_{M/GB} > 0 \\ \eta_{M/GB} T_{M/GB}\omega_o - \frac{\frac{R}{1+R} T_e \omega_{M/GA}}{\eta_{M/GA}} & T_{M/GB} < 0 \end{cases}, \tag{2.16}$$

can be calculated. At the "mechanical point" speed ratio, the power from the engine is purely transmitted to the ring gear resulting in no *M/GA* power flow. For $SR = SR_{mech}$, battery power,

$$P_B = \begin{cases} \frac{T_{M/GB}\omega_o}{\eta_{M/GB}} & T_{M/GB} > 0 \\ \eta_{M/GB} T_{M/GB}\omega_o & T_{M/GB} > 0 \end{cases}, \tag{2.17}$$

is defined based on *M/GB* functionality.

2.2 General Motors Allison Hybrid System II

The GM AHS-II powertrain is capable of operating in input-split or compound-split EVT modes as well as four FG configurations. Multi-mode operation is enabled by using multiple planetary gearsets and mode changing clutches. The GM AHS-II powertrain is composed of several key components: battery, IC engine, two braking clutches, two rotating transfer clutches, two inverters, two motor-generator EMs, and two planetary PSDs (*PG1* and *PG2*). The key components of the FWD GM AHS-II powertrain and positive power conventions assumed throughout this analysis are displayed in Figure 2.3.

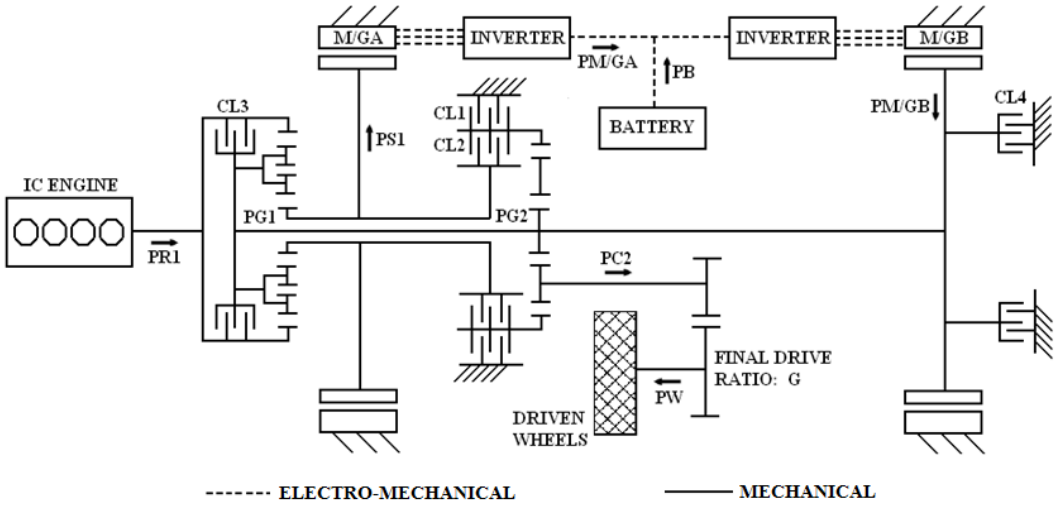

Figure 2.3: Cut-away of the GM AHS-II powertrain

The first PSD, labeled *PG1* in Figure 2.3, is a compound planetary gearset with three sets of two pinion gears mounted on a single carrier. The second PSD, *PG2*, is a simple planetary gearset with three single pinion gears between the sun and ring gears as used in THS-II transmission. Power is input from the IC engine which is continuously connected to the ring gear of *PG1*. Power is transmitted from the carrier gear of *PG1* to the sun gear

of *PG2* through a rigid connection. *M/GA* is rigidly connected to the sun gear of *PG1* and *M/GB* is rigidly connected to both the *PG1* carrier gear and *PG2* sun gear. The rotational speed of the *PG2* carrier gear is proportional to vehicle speed by the final-drive ratio *G*. Thus, for any prescribed vehicle speed, the rotational speed of the *PG2* carrier $\omega_o = \omega_{C2}$ is known. The four clutches displayed in Figure 2.3 allow additional connections required to implement any of six operating modes. Table 2.1 displays the operating modes and the respective clutch states that enable each.

Table 2.1: Clutches associated with mode selection

Mode	***CL1***	***CL2***	***CL3***	***CL4***
EVT-1	Engaged			
EVT-2		Engaged		
FG-1	Engaged		Engaged	
FG-2	Engaged	Engaged		
FG-3		Engaged	Engaged	
FG-4		Engaged		Engaged

Like the THS-II powertrain, both EMs are capable of bi-directional energy flow and the battery is an energy buffer that cannot be externally recharged. Therefore, SOC must be maintained within operational limits or the integrity of the battery is jeopardized.

The addition of a second PSD, a three axis compound planetary gearset with three sets of two pinion gears mounted on a single carrier gear in Figure 2.4, enables the second EVT mode of the GM AHS-II powertrain.

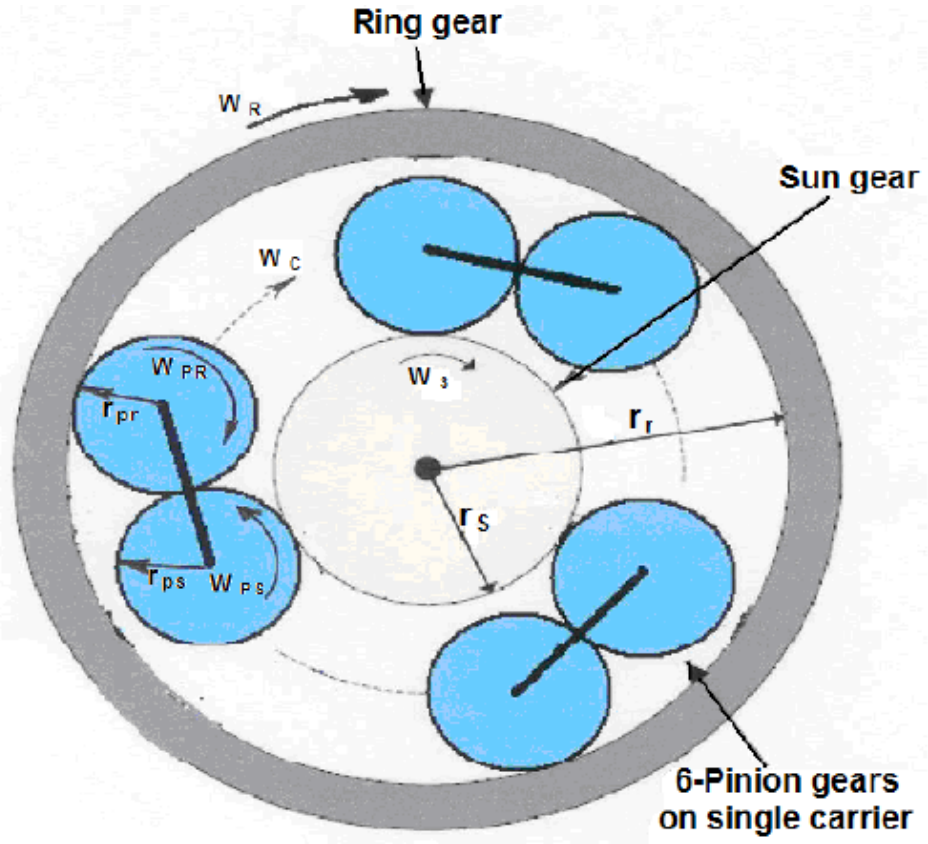

Figure 2.4: *PG1* in the GM AHS-II powertrain is a compound planetary gearset, reproduced from [32].

The second PSD enables additional degrees of freedom and advantageous operating modes. The characteristic ratio R_1 for the compound planetary gearset and R_2 the simple planetary gearset in Figure 2.3 are defined by,

$$R_1 = \frac{r_{1,sun}}{r_{1,ring}} = \frac{N_{1,sun}}{N_{1,ring}}, \tag{2.18}$$

$$R_2 = \frac{r_{2,sun}}{r_{2,ring}} = \frac{N_{2,sun}}{N_{2,ring}}, \tag{2.19}$$

where *r* is the radius and *N* is the number of teeth on the respective gears. Subscripts *1* and *2* denote the compound and simple planetary gearsets. Torque constraints on the

planetaries are derived by imposing a power balance neglecting gearset accelerations, reducing to the steady-state torque relationships,

$$T_{C1} = -(1 - R_1)T_{R1} = \frac{1-R_1}{R_1}T_{S1}, \tag{2.20}$$

$$T_{C2} = -(1 + R_2)T_{R2} = -\frac{1+R_2}{R_2}T_{S2}, \tag{2.21}$$

where T_C, T_R, and T_S are the carrier, ring, and sun gear torques for the respective gearsets. Kinematic speed constraints based on equal speeds at points of contact where meshing occurs exist,

$$\omega_{C1} = \frac{1}{1-R_1}\omega_{R1} - \frac{R_1}{1-R_1}\omega_{S1}, \tag{2.22}$$

$$\omega_{C2} = \frac{1}{1+R_2}\omega_{R2} + \frac{R_2}{1+R_2}\omega_{S2}, \tag{2.23}$$

such that ω_C, ω_R, and ω_S are the carrier, ring, and sun gear rotational velocities of the respective gearsets. From the torque and speed constraints of each gearset, it can be noted there is one independent torque and two independent speeds constraining the power delivery through the three branches of each PSD. The relevant facts discussed in Section 2.1 regarding simple planetary gearsets also apply to compound planetary gearsets.

2.2.1 General Motors Allison Hybrid System II Modes of Operation

Power flow through each branch of the PSDs is modeled by component efficiencies and constraining speed and torque equations. The IC engine is characterized by its thermal efficiency and the EMs are characterized by their efficiency maps, inverter losses included. The mode of operation dictates the constraining speed and torque equations of the EMs (motoring versus generating). The constraining component speed and torque equations are derived in terms of the IC engine input and *PG2* carrier output for use in simulation. Engine power is a control strategy degree of freedom and *PG2* carrier gear

power is dependent on the drive-cycle. The operation of the two electrically variable modes will be detailed next.

Mode *EVT-1* corresponds to input-split operation and is very similar to THS-II operation. *PG1* splits input engine power between the mechanical and electro-mechanical power path. This dual-mode hybrid powertrain is designed to shift modes according to changes in the driving environment at a synchronous shift speed ratio between the two EVT modes. As vehicle speed increases for a given engine speed, energy flow through the electro-mechanical path reverses undesirably. Undesirable reversal of energy flow through the electro-mechanical path is prevented by switching to mode *EVT-2*. *EVT-2* corresponds to compound-split operation in which *PG1* splits input engine power and *PG2* combines the split mechanical and electro-mechanical power paths before the final-drive gearing. The GM AHS-II transmission also has four FG ratios that provide a purely mechanical power path from the IC engine to the driven wheels without the need for electro-mechanical power. FG operation also has the flexibility of utilizing one or both EMs to contribute to the tractive effort by motoring or generating. FG operation improves towing, climbing and maximum acceleration performance but constrains engine speed to one of four values for a given vehicle speed. Regardless of the transmission speed ratio, *FG-2* and *FG-4* correlate to "mechanical point" speed ratios such that *M/GA* and *M/GB* respectively do not rotate. By not transmitting power, the EMs are not subject to energy conversion losses. By holding *M/GA* stationary in *FG-2*, *FG-2* enables a seamless transition amongst EVT modes.

<u>EVT-1</u>

In mode *EVT-1*, input-split operation is achieved by locking the ring gear of *PG2* with *CL1*. The input engine power is split by *PG1* while *PG2* provides torque multiplication by serving as a conventional two terminal gearset. While operating in *EVT-1*, the constraining speed equations are,

$$\omega_{M/GA} = \frac{1}{R_1}\omega_e - \frac{(1-R_1)(1+R_2)}{R_1 R_2}\omega_o, \tag{2.24}$$

$$\omega_{M/GB} = \frac{1+R_2}{R_2}\omega_o, \tag{2.25}$$

and the torque constraints are,

$$T_{M/GA} = -R_1 T_e, \tag{2.26}$$

$$T_{M/GB} = -(1-R_1)T_e + \frac{R_2}{1+R_2}T_o. \tag{2.27}$$

EVT-2

In mode *EVT-2*, compound-split operation is achieved by locking the ring gear of *PG2* to the sun gear of *PG1* with *CL2*. The power is split by *PG1* at the input and combined by *PG2* at the output. While operating in *EVT-2*, the constraining speed equations are,

$$\omega_{M/GA} = -\frac{R_2}{1-R_1-R_1R_2}\omega_e + \frac{(1-R_1)(1+R_2)}{1-R_1-R_1R_2}\omega_o, \tag{2.28}$$

$$\omega_{M/GB} = \frac{1}{1-R_1-R_1R_2}\omega_e - \frac{R_1(1+R_2)}{1-R_1-R_1R_2}\omega_o, \tag{2.29}$$

while the torque constraints are,

$$T_{M/GA} = -R_1 T_e + \frac{1}{1+R_2}T_o, \tag{2.30}$$

$$T_{M/GB} = -(1-R_1)T_e + \frac{R_2}{1+R_2}T_o. \tag{2.31}$$

The preferred direction of power flow though the EMs is reversed when operating in *EVT-2* relative to *EVT-1*.

FG-1

PG1 is locked by *CL3* allowing direct drive and the ring gear of *PG2* is held stationary by *CL1*, providing speed reduction. *FG1* enables the greatest FG ratio and is best utilized for maximum FG acceleration. Derived from the planetary gearsets constraining equations, *FG-1* angular velocities are,

$$\omega_e = \omega_{M/GA} = \omega_{M/GB} = \frac{1+R_2}{R_2}\omega_o, \tag{2.32}$$

and the torque constraint is,

$$T_o = \frac{1+R_2}{R_2}(T_e + T_{M/GA} + T_{M/GB}). \tag{2.33}$$

FG-2

Through the use of *CL1* and *CL2*, *FG-2* is the synchronous shift mode allowing a transition between *EVT-1* and *EVT*-2 since *M/GA* is stationary. From *FG-2*, disengaging either *CL1* or *CL2* enables one of the EVT modes. Derived from the planetary gearsets constraining equations, *FG-2* angular velocities are constrained such that,

$$\omega_e = \frac{(1-R_1)(1+R_2)}{R_2}\omega_o, \tag{2.34}$$

$$\omega_{M/GA} = 0, \tag{2.35}$$

$$\omega_{M/GB} = \frac{1+R_2}{R_2}\omega_o, \tag{2.36}$$

while the torque constraint is,

$$T_o = \frac{(1-R_1)(1+R_2)}{R_2}T_e + \frac{1+R_2}{R_2}T_{M/GB}. \tag{2.37}$$

FG-3

All three terminals of *PG1* and *PG2* are locked by engaging *CL3* and *CL2,* allowing direct drive between the engine and wheels. *FG-3* is ideal for hill climbing and towing.

Derived from the planetary gearsets constraining equations, *FG-3* angular velocities can be constrained as,

$$\omega_e = \omega_{M/GA} = \omega_{M/GB} = \omega_o, \tag{2.38}$$

and the torque constraint is,

$$T_o = T_e + T_{M/GA} + T_{M/GB}. \tag{2.39}$$

FG-4

CL2 is engaged, locking *PG1* ring gear enabling overdrive and *PG2* sun gear is held stationary by *CL4*. *FG4* is best used for FG constant vehicle speed cruising. Since *M/GB* is stationary regardless of the operating conditions, *FG-4* operation occurs at the second "mechanical point" speed ratio of the GM AHS-II architecture. Since *M/GB* does not rotate, no energy conversion loses are experienced by the EM. Derived from the planetary gearsets constraining equations, *FG-4* angular velocity can be constrained,

$$\omega_e = R_1(1 + R_2)\omega_o, \tag{2.40}$$

$$\omega_{M/GA} = (1 + R_2)\omega_o, \tag{2.41}$$

$$\omega_{M/GB} = 0, \tag{2.42}$$

while the torque constraint is,

$$T_o = R_1(1 + R_2)T_e + (1 + R_2)T_{M/GA}, \tag{2.43}$$

As in the THS-II architecture, the speed ratio is an important measure that dictates the preferred direction of power flow through the EMs in the GM AHS-II powertrain. From Equation (2.24) and Equation (2.25) describing *EVT-1* operation, there are two speed ratios at which one of the EMs does not rotate,

$$SR = \frac{\omega_e}{\omega_o} = \begin{cases} \frac{(1-R_1)(1+R_2)}{R_2} & \omega_{M/GA} = 0 \\ 0 & \omega_o = \omega_{M/GB} = 0 \end{cases}. \tag{2.44}$$

From Equation (2.28) and Equation (2.29) describing component operation in *EVT-2*, there are two speed ratios at which one of the EMs does not rotate,

$$SR = \frac{\omega_e}{\omega_o} = \begin{cases} \frac{(1-R_1)(1+R_2)}{R_2} & \omega_{M/GA} = 0 \\ R_1(1+R_2) & \omega_{M/GB} = 0 \end{cases}. \quad (2.45)$$

From comparison of *EVT-1* and *EVT-2* "mechanical point" speed ratios, a common synchronous shift speed ratio exists. This speed ratio corresponds to *FG-2* operation, enabling shifting between *EVT-1* and *EVT-2* because *M/GA* is not rotating. Shifting from *EVT-1* to *EVT-2* maintains the desired direction of power through the EMs, minimizing undesirable energy conversion losses.

2.3 Simulation Approach

BLS utilizes backward-looking drive-cycle based calculations to determine the required mechanical power at the driven wheels of the simulated powertrains. To enable a backward-looking approach, a drive-cycle must be defined that specifies vehicle velocity $V(t)$ over the cycle's time interval $t \in [0, T]$. A vehicle is defined in terms of the parameters needed for road-load calculations: ambient air density ρ_{air}, drag coefficient C_d, frontal area A_f, grade α, gravity g, vehicle mass M, and rolling resistance coefficient μ. The force at the driven wheels F_W,

$$F_W = \mu M g cos\alpha + \frac{1}{2}\rho_{air} A_f C_d V^2 + M\frac{\partial V}{\partial t}, \quad (2.46)$$

required to follow the applied drive-cycle can be used to calculate the demanded torque and power for a given speed at every discrete time of the cycle. Throughout this analysis the grade of the drive-cycle is assumed to be inclined zero degrees and rotational inertia of shafts, gears, etc. is ignored. For an EVT, mass factor is not constant; it would vary with transmission input-output SR. This extra complexity arises due to the fact that there

are two independent speeds for an EVT. Although both powertrains are modeled with different IC engines and EMs, both are on the same mid-size sedan vehicle body. The THS-II one-mode powertrain employs a 1.5 L four cylinder IC engine while the GM AHS-II powertrain employs a 1.6 L four cylinder IC engine. The characteristic ratios defining the transmissions are mated to the fuel consumption characteristics of the respective engine's BSFC map. An ill-defined characteristic ratio R could lead to potentially inefficient IC engine operation. For the sake of comparison, these powertrains were modeled on the same vehicle chassis but with their native powertrain components.

The road-load calculation results in the required mechanical power at the driven wheels $P_W(V(t))$ consisting of force terms resulting from rolling friction, aerodynamic drag, and vehicle acceleration. This chapter will define an admissible region of the IC engine map such that the EMs are operated in their usable range and the required mechanical power is delivered to the driven wheels. The BSFC maps for both powertrains are not presented here; however, they can be found in [12] for the Toyota powertrain and [34] for the GM powertrain. For both architectures, the rotational speeds of the EMs are functions of the input engine speed and output vehicle speed. For a given vehicle speed, an admissible IC engine speed range can be defined such that the EMs are not over-sped. In both architectures, the IC engine and EMs combine to deliver the required mechanical power at the driven wheels. In order to deliver the demanded power, an admissible engine torque range can be defined based on the magnitude-limited power contributions of the electro-mechanical path. At each time instant of the drive-cycle, the two drive-cycle dependent admissible requirements, i) IC engine rotational speed range and ii) IC engine

torque range, define a restricted region of the IC engine map. By developing the constraining speed and torque equations for both architectures in terms of the transmission input and output, each admissible engine operating point fully constrains power delivery within both architectures. Any point within the admissible region of the engine map ensures proper operation of the EMs and delivery of the demanded driver power to the driven wheels. This chapter exhaustively searches all admissible input operating points and selects the operating state that minimizes an instantaneous cost function at each time instant of the drive-cycle.

2.3.1 THS-II Admissible IC Engine Rotational Speed Range

By replacing *M/GA* rotational speed in Equation (2.5) with both the maximum and minimum *M/GA* speed limits, the upper and lower limits of the speed ratio can be obtained. By manipulating Equation (2.6), the upper and lower limits of the admissible engine speed can therefore be obtained and are plotted in Figure 2.5.

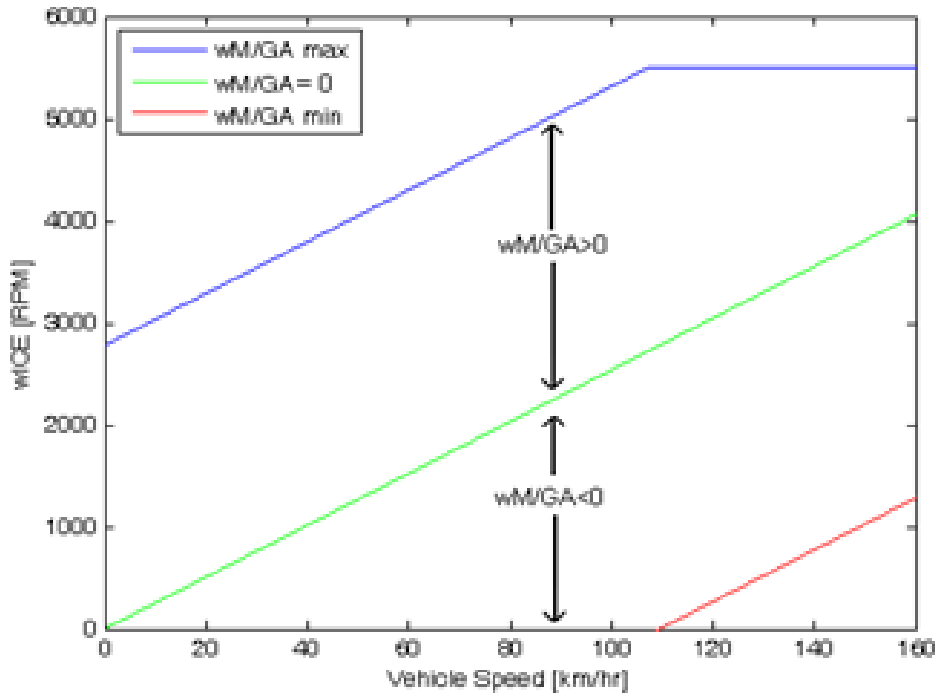

Figure 2.5: Admissible IC engine speed range for THS-II architecture

In Figure 2.5 the blue, green, and red lines represent *M/GA* rotating at maximum speed, zero rotational speed, and minimum speeds respectively. Resulting from the kinematics of the PSD, the IC engine must always operate within the admissible speed range defined in Figure 2.5 for a given vehicle speed to guarantee proper *M/GA* operation.

2.3.2 GM AHS-II Admissible IC Engine Rotational Speed Range

The speed ratio of the GM AHS-II powertrain operating in *EVT-1* and *EVT-2* is defined in Equation (2.44) and Equation (2.45). By replacing the rotational speed of the EMs with their maximum and minimum speed limits, the upper and lower limits of the speed ratios can be obtained. By manipulating these speed ratios, the admissible IC engine rotational speed range can be defined for *EVT-1* and *EVT-2* as summarized in Figure 2.6.

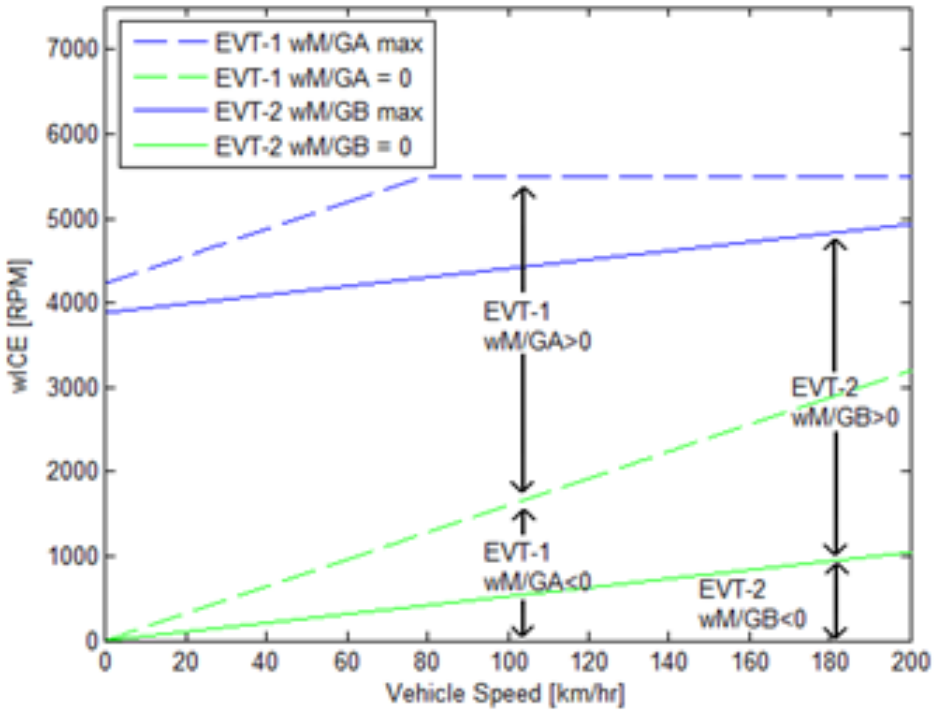

Figure 2.6: Admissible IC engine speed range for GM AHS-II architecture

Power circulation loops and undesirable energy conversion losses can be eliminated in the GM AHS-II dual-mode transmission by adaptively switching between *EVT-1* and *EVT-2*. The selected EVT mode dictates the operation (motoring versus generating) of the EMs and the direction of electro-mechanical power flow. While operating in a FG mode, engine speed is constrained to one of four options for a given vehicle speed. In order to guarantee proper EM operation, the IC engine must always rotate within the admissible range defined by the operating mode for a specified vehicle speed.

In order to maintain charge sustaining operation and battery integrity, battery power must vary based on SOC. If the IC engine delivers more power than is required at the driven wheels, the excess can be stored in the battery. At critically low SOC, a critical battery

power generation rate $P_{B,low}$ must be employed in order to increase SOC at that particular time instant of the drive-cycle. SOC must be built in order to be used advantageously in future time steps of the cycle. As SOC increases, more electro-mechanical and battery power is available to be delivered to the wheels. At critically high SOC the battery cannot store additional electrical energy; and charge cannot be regenerated even if beneficial. Therefore, a critical battery power delivery rate $P_{B,high}$ must be employed in order to decrease SOC at that instant of the drive-cycle. The proposed idea of defining an allowable battery power range based on SOC can be visualized in Figure 2.7.

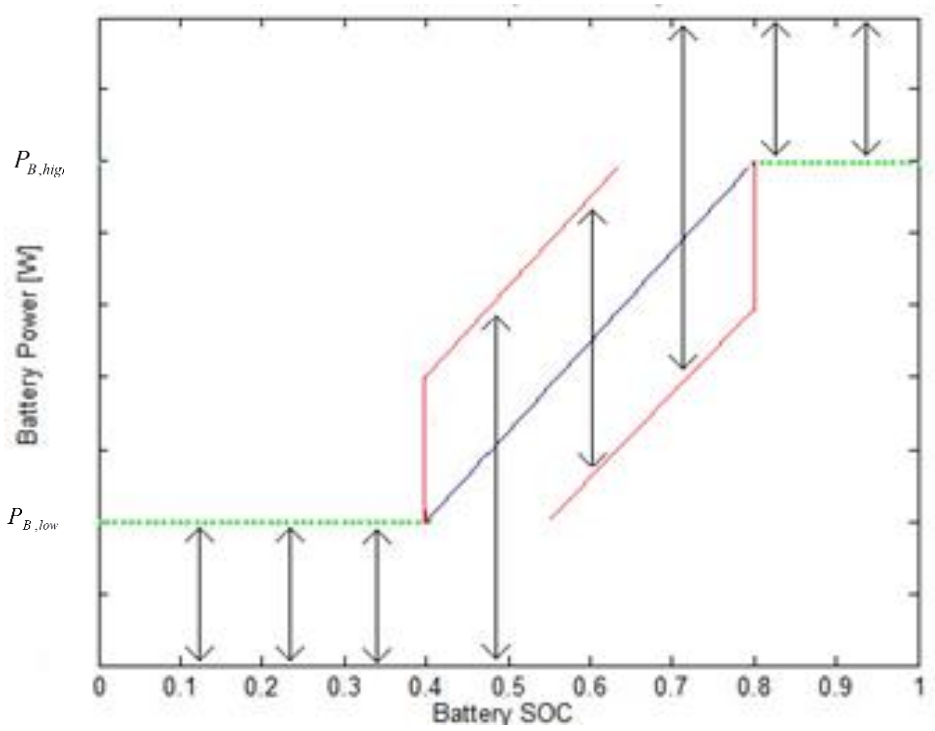

Figure 2.7: Allowable battery power varies with SOC in order to maintain charge sustaining operation.

From the concept of constraining battery power at critical SOC, a continuum of battery power can connect the extreme SOC conditions and be applied over the battery's usable SOC range. The allowable battery power width over the operational SOC range displayed in Figure 2.7 dictates how much power can be drawn or delivered to the battery. This continuum strategy informs the determination of a cost function as detailed below.

2.3.3 Two-Term Cost Function

The required mechanical power at the driven wheels is determined by the drive-cycle, but the ratio of engine to battery power is a control strategy degree of freedom. To enable a comparative study between the two power paths to the wheels, this analysis considers a multi-objective cost function *C*,

$$C = P_f + sP_B, \tag{2.47}$$

where $P_f = H_l \dot{m}_f$ is the power obtained from burning liquid fuel in the internal combustion engine, H_l is the heating value of the fuel, $\dot{m}_f$ is the flow rate of fuel into the engine, and *s* is the equivalence factor used to weight battery power based on battery state-of-charge. This paper implements two forms of the electric power equivalence factor *s*, both linear and inverse tangent.

$$s_{linear}(x)_j = \begin{cases} s_{max} & x \le x_{min} \\ s_{min} & x \ge x_{max} \\ ax + b & x_{min} \le x \le x_{max} \end{cases}, \tag{2.48}$$

$$s_{tan^{-1}}(x)_j = \begin{cases} s_{max} & x \le x_{min} \\ s_{min} & x \ge x_{max} \\ (tan^{-1}(x) + c)d & x_{min} \le x \le x_{max} \end{cases}, \tag{2.49}$$

In Equation (2.48) and Equation (2.49), the subscript *j* denotes the time step of the drive-cycle and *x* represents the battery state-of-charge. An electric power equivalence factor *s*

is assigned to each discrete time of the drive-cycle. The electric power equivalence factor *s* is inversely proportionate to the allowable battery power range and varies with SOC as shown in Figure 2.8.

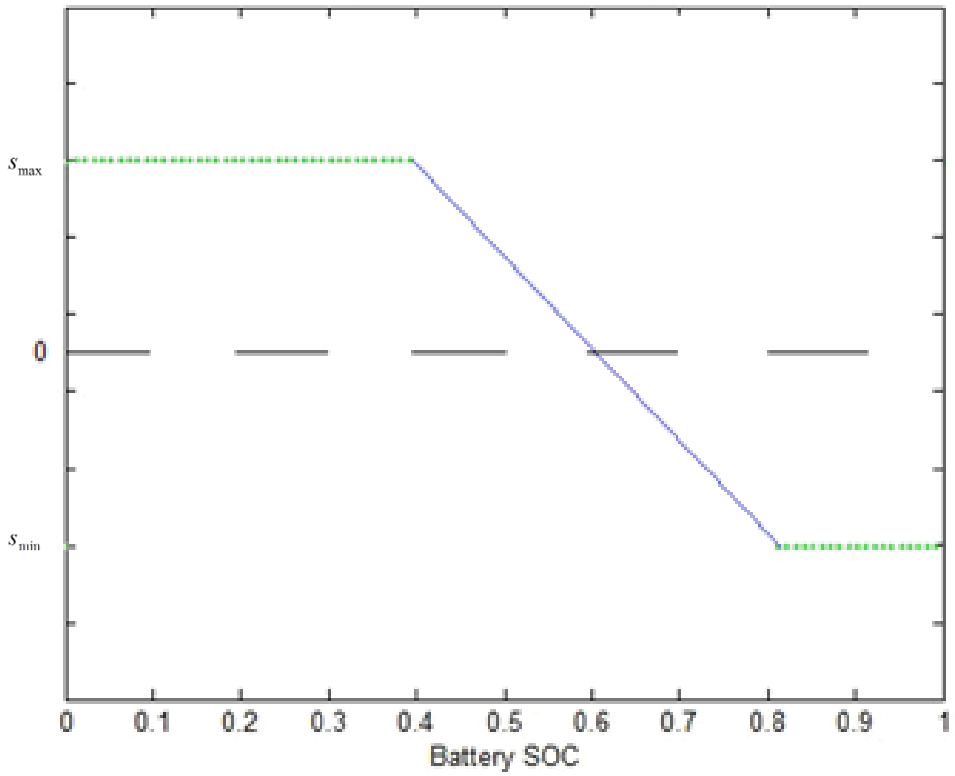

Figure 2.8: Linear electric power equivalence factor *s* varies with SOC in order to maintain charge sustaining operation.

By defining the constraining EM speed and torque equations in terms of the drive-cycle dependent road-load conditions and an IC engine operating point, each admissible engine map point results in an ensuing battery power. The design approach is to exhaustively search all admissible states and to minimize the instantaneous cost function in Equation (2.47) at each time instant of the drive-cycle. Minimizing the cost function results in the

fully constrained system operating states such that the driver power demand is satisfied, SOC bounds are adhered to, and fuel consumption is minimized. Intelligent power delivery throughout this analysis was designed to avoid inefficient power circulation loops.

2.4 Results

The THS-II and GM AHS-II simulation results are presented throughout this section using a combined urban-rural drive-cycle. A drive-cycle combined of rural and urban cycles is created to produce a unified index of fuel economy. This driving schedule is the following EPA drive-cycles combined in series: UDDS, US06, HWFET, IM240, NYCC, LA92, UDDS, HWFET, UDDS, and UDDS [35]. The vehicle velocity $V(t)$ is specified over the cycle's time interval $t \in [0, T]$ and the grade of the cycle is assumed to be inclined zero degrees. This drive-cycle has a total length of 71.3 miles and is displayed in Figure A.1 of Appendix A. Table 2.2 displays the miles per gallon fuel economy estimates that were obtained from the backward-looking simulations over the combined urban-rural drive-cycle following the optimization described.

Table 2.2: BLS Fuel economy estimates over unified drive-cycle

Weighted Battery Power Equivalence Factor	Fuel Economy (MPG)
THS-II	
Linear	51.04
Inverse Tangent	54.26
GM AHS-II	
Linear	52.02
Inverse Tangent	54.90

Throughout the unified drive-cycle backward-looking simulations, the time spent by the GM AHS-II architecture in each mode can be summarized as shown in Figure 2.9.

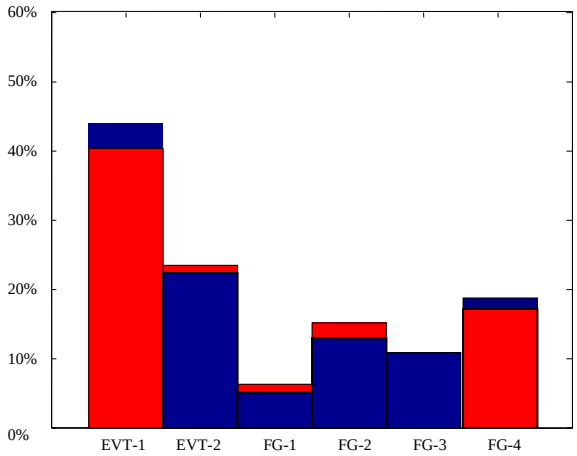

Figure 2.9: GM AHS-II percent operation spent in each operating mode

In Figure 2.9, the red bar graph represents the linearly weighted battery power and the blue bar graph represents the inverse tangent weighted battery power. Both electric power equivalence factors spend the same percentage of operating time in *FG-3*. The control parameters that affect the cost of battery power usage *s*, dictate battery power delivery for a given state-of-charge and ultimately operational mode selection. Note that selected operational states do not necessarily correspond to the minimum BSFC point on the engine map or the highest efficiency EM usage. Instantaneous battery power allows the system to operate at its maximum overall efficiency and ultimately maximize fuel economy. The trade-off of achieving charge sustaining operation versus fuel consumption characteristics are to be addressed next.

Battery power consumption affects the fuel economy characteristics of both powertrains. Making the electric power equivalence factor *s* less dominant expands the resulting operational battery power range, allowing more power to be drawn from or delivered to the battery. By allowing more power to be drawn from the battery, the electro-mechanical propulsion has more flexibility in assisting the engine in reaching higher efficiency operating regions. As a consequence, SOC has the ability to fluctuate more and operation becomes less charge sustaining. If electro-mechanical propulsion is over-utilized, eventually a critical SOC will be reached as shown in Figure 2.10 circled in red. Figures 2.10 and 2.11 display the linear electric equivalent factor fits in green and the inverse tangent fits in red around the operating points resulting from the cost function. As will be shown, the inverse tangent method achieves better fuel economy by advantageously using stored battery power over the SOC range.

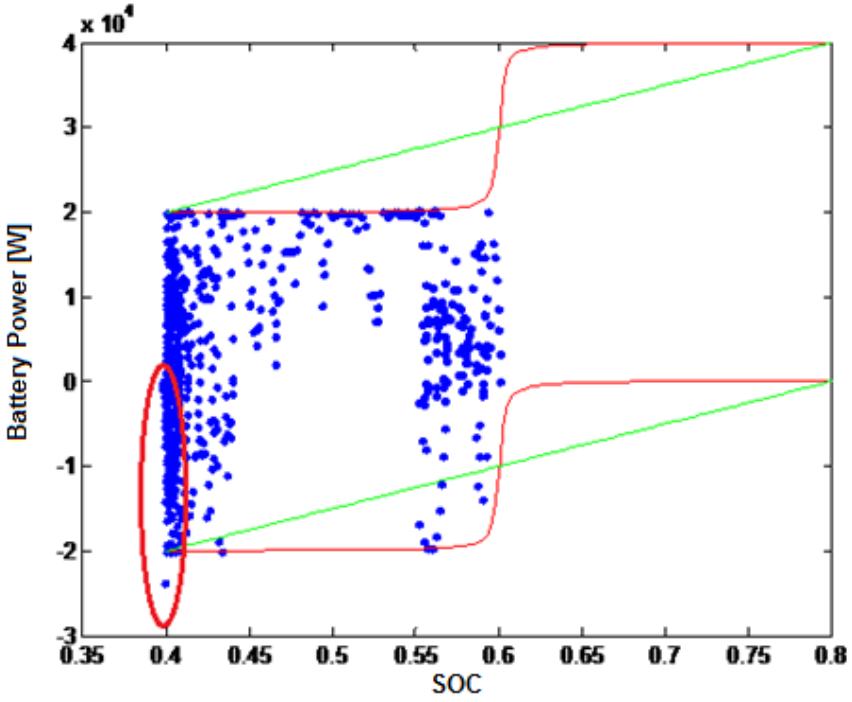

Figure 2.10: Less prevalent electric power equivalence factor *s*

Circled in red in Figure 2.10 are examples of inefficient IC engine operation required to increase battery SOC. At critically low SOC, an inefficient engine operating point may be selected to increase SOC. Making the electric power equivalence factor *s* more dominant discourages battery power usage. However, if too dominant, the ensuing selected battery range is restricted, drawing and delivering less energy to the battery. By assigning a higher cost to using stored battery power, the electro-mechanical propulsion cannot be fully utilized. Figure 2.11 displays an overly dominant equivalence factor *s*, where SOC does not have the ability to fluctuate.

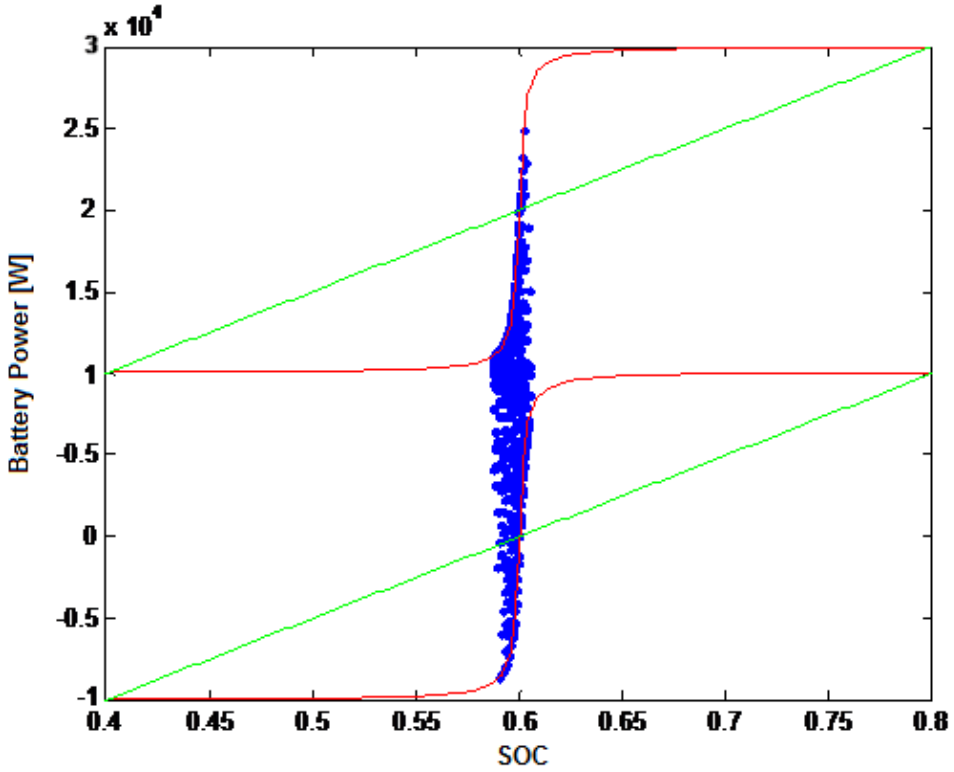

Figure 2.11: Heavily weighted electric power equivalence factor *s* restricts battery power

In order to quantitatively evaluate the ability to fluctuate SOC and sustain charge, a charge sustaining (CS) index *I* was determined,

$$I = \frac{\sum_{j=1}^{N} |x(j) - x_i|}{N}. \tag{2.50}$$

Influencing *I* can be accomplished by altering the control parameters *a* and *b* in Equation (2.48) and *c* and *d* in Equation (2.49). The control parameters *a*, *b*, *c*, and *d* are varied such that the selected battery power points correspond to 5% increments of the total available battery power. The inverse tangent fits displayed in Figures 2.10 and 2.11 are used to show the width of selected battery powers resulting from the cost function. If *I* is constrained too tightly or loosely, the system may not be able to fully take advantage of electro-mechanical assistance. The green vertical lines in Figures 2.12 and 2.13 display *I* resulting in maximized fuel economy over the unified drive-cycle for the THS-II architecture.

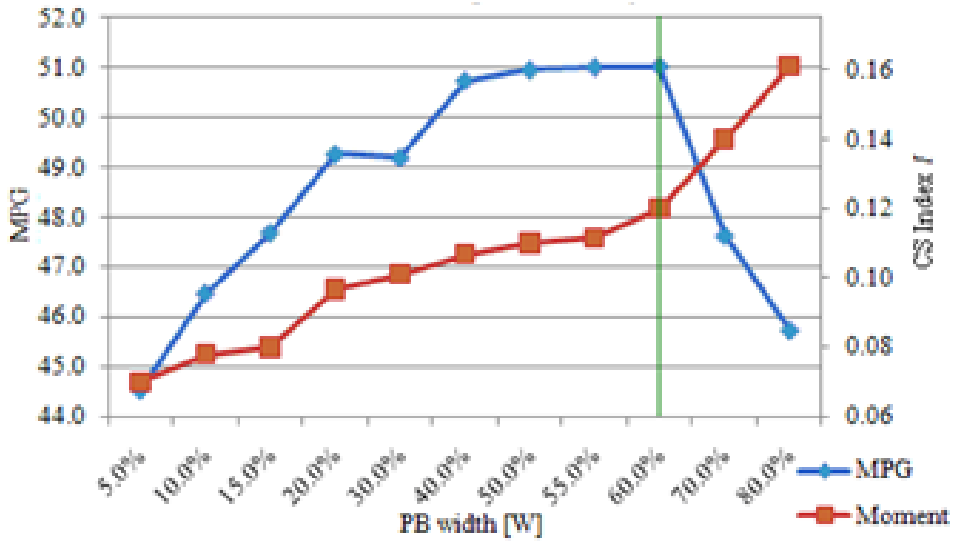

Figure 2.12: THS-II linear weighted battery power results

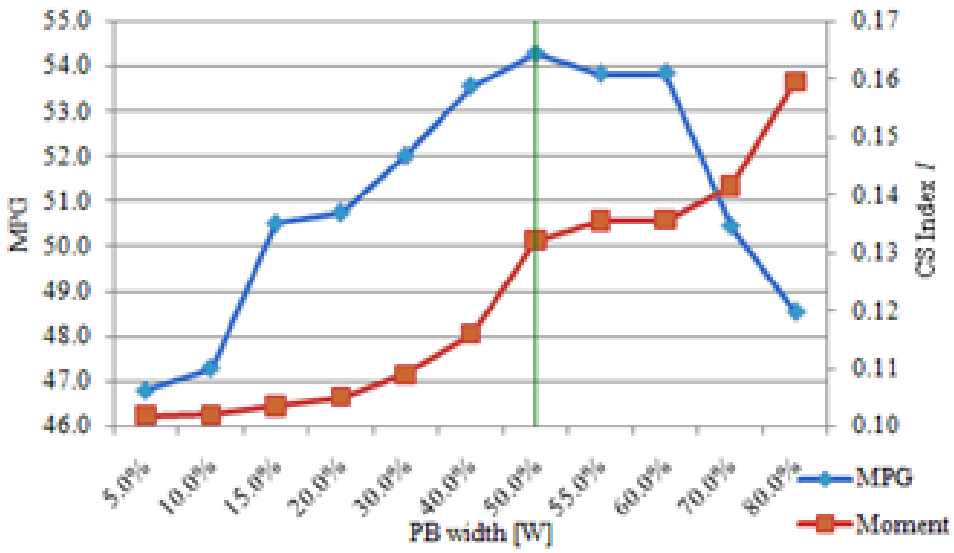

Figure 2.13: THS-II inverse tangent weighted battery power results

The green vertical lines in Figures 2.14 and 2.15 display the CS index resulting in maximized fuel economy over the unified drive-cycle for the GM AHS-II architecture.

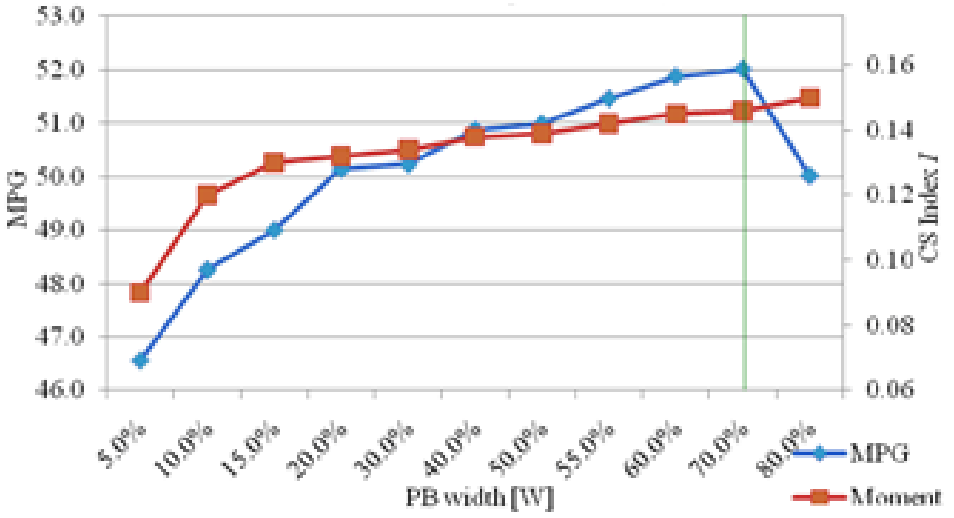

Figure 2.14: GM AHS-II linear weighted battery power results

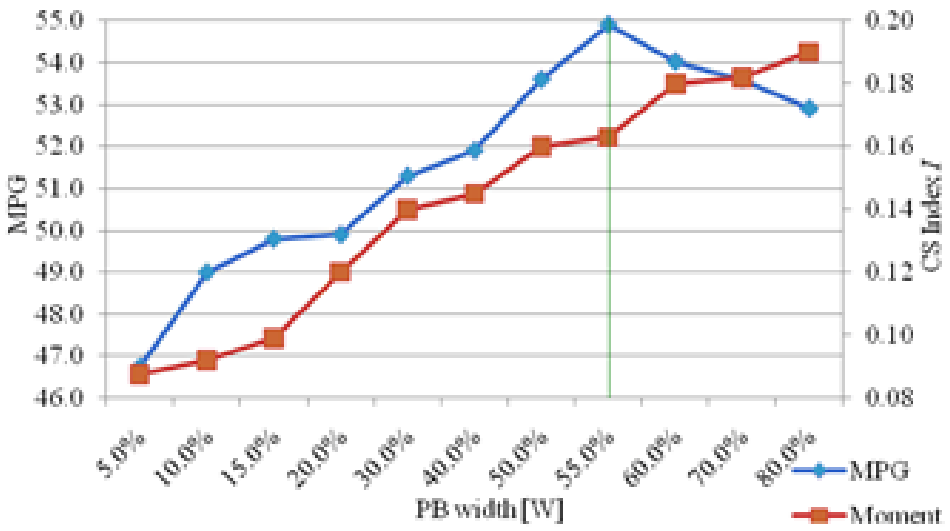

Figure 2.15: GM AHS-II inverse tangent weighted battery power results

From Figures 2.11-2.15, the best performing power management strategy exists at the battery power width where the CS index *I* abruptly increases and the fuel economy diminishes. The inflection point of *I* in Figures 2.11-15 implies battery power management strategies that result in minimized fuel consumption. By over or under-utilizing electro-mechanical propulsion, a system may not operate at its maximum efficiency. Therefore this analysis presents a performance tradeoff between utilizing electro-mechanical propulsion and fuel consumption.

The added flexibility of a second EVT mode and four FG configurations contribute to the increased fuel economy performance of the GM AHS-II powertrain. By taking advantage of a second operating configuration, the EM angular velocities of the dual-mode system are significantly reduced compared to the one-mode system. By shifting between EVT modes, GM AHS-II electro-mechanical power can be delivered in a more desirable fashion by eliminating electro-mechanical conversion losses and results in more

efficient system operation. The direction of angular velocity, and hence electro-mechanical power, of *M/GA* and *M/GB* in *EVT-1* is reversed relative to *EVT-2* as seen in Figure 2.16.

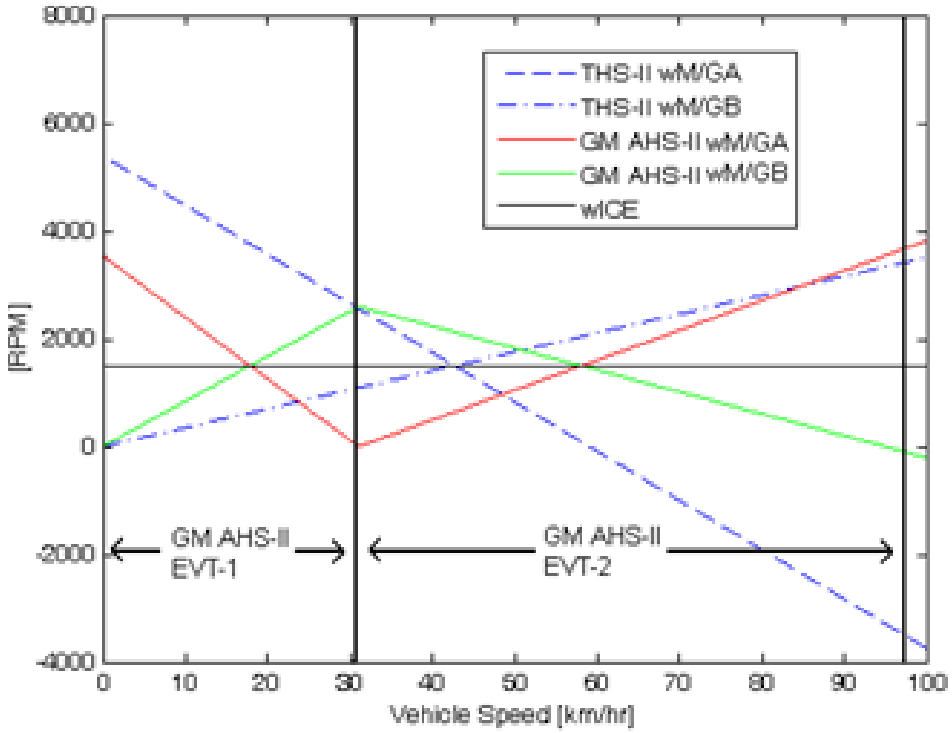

Figure 2.16: GM AHS-II powertrain maintains positive electro-mechanical power by shifting amongst EVT modes, shown ω_e=1500 RPM

By shifting EVT modes and switching direction of the EMs' rotational speeds, GM AHS-II energy conversion losses are minimized resulting in increased power delivery efficiency. Therefore GM AHS-II electro-mechanical power delivery is more efficient and requires less battery power relative to the THS-II architecture.

A higher-order electric power equivalence factor *s* results in increased fuel economy and overall system efficiency for both architectures. From Figures 2.12 and 2.13, THS-II inverse tangent weighted electric consumption consumes less battery power than the linear factor. This is consistent with the results depicted in Figures 2.14 and 2.15 for the GM AHS-II powertrain. This is because the higher-order form of *s* delivers battery power in a more desirable fashion over the usable SOC range. From Figures 2.10 and 2.11, it can be noted that at low SOC inverse tangent electric power equivalence factor allows more charge to be regenerated and less to be delivered from the battery. At high SOC, the inverse tangent electric power equivalence factor allows more charge to be deliverd from the battery and less to be regenerated. These constraints promote charge sustaining operation and demand less electric power consumption.

From Figure 2.9, the manner in which battery power is used determines the operating mode of the GM AHS-II system. Inverse tangent battery power allows the system to operate more frequently in *EVT-1* and operate via pure electric propulsion. By spending more time in *EVT-1*, the increased fuel economy of the inverse tangent weighted battery power can be justified. To compensate for less time spent in *EVT*-1, the linearly weighted battery power operates more frequently in *FG-1*. *FG-1* is the highest FG ratio and is best suited for start and stop operation, the most inefficient pure IC engine operating condition. By operating more frequently in *FG-1* relative to *EVT-1*, the linearly weighted battery power simulation results in decreased fuel economy.

2.4.1 Summary

In this chapter the one-mode THS-II and two-mode GM AHS-II powertrains were modeled on a common mid-size sedan vehicle chassis. The powertrains have different transmissions, EMs, and IC engines. Resulting from backward-looking simulation, it is shown that one-mode architectures are limited by one design variable *R*, one ensuing "mechanical point" speed ratio, and one transmission configuration. One transmission configuration increases negative energy flow through the EMs, resulting in increased energy conversion losses. The energy conversion losses in the THS-II architecture demand larger, more expensive, and more powerful electro-mechanical propulsion components relative to the GM AHS-II architecture. On the contrary, the THS-II transmission has less packaging considerations without the need of a second planetary gearset and clutches.

The addition of a second "mechanical point" speed ratio and another transmission configuration enables more desirable electro-mechanical energy flow and more efficient EM operation over all road-load conditions. With the capability of operating the EMs more efficiently and the added flexibility of the FG operating modes, the two-mode GM AHS-II powertrain displays a modest increase in fuel economy over the one-mode THS-II powertrain. As a tradeoff, increased performance metrics come with increased component costs and packaging complexity.

CHAPTER 3

POWER-SPLIT HEV CONTROL STRATEGY DEVELOPMENT WITH REFINED ENGINE TRANSIENTS

The supervisory control design approach used in Chapter 2 is summarized in Figure 3.1 with additional notation useful for the present chapter. At each instant of the drive-cycle, an input-state $\boldsymbol{S_{in}} = [T_o\ \omega_o\ \mathrm{SOC}]$ is defined containing the road-load condition (transmission output torque T_o and transmission output speed ω_o) and battery SOC. The road-load condition, constraints on engine and transmission rotational speeds, and the achievable transmission SRs define kinematically admissible regions of the IC engine BSFC and torque maps. Each admissible engine operating point then contributes to an output-state $\boldsymbol{S_{out}} = [\omega_e\ T_e\ T_{M/GB}]$ containing IC engine speed ω_e, IC engine torque T_e, and output motor-generator torque $T_{M/GB}$. The goal of the supervisory controller is to choose an $\boldsymbol{S_{out}}$, for each $\boldsymbol{S_{in}}$, which maximizes the efficient operation of the powertrain. Note that this output state may be one requiring excess power storage in the ESS. The approach employed is to then exhaustively search all kinematically admissible input operating points and to then minimize a two-term instantaneous cost function. The electric power equivalence factor *s* is used to balance fuel and battery power consumption. By varying the form of *s*, different battery power management strategies can be assessed. In Chapter 2, *s* was varied to find battery power management strategies that resulted in maximized FE.

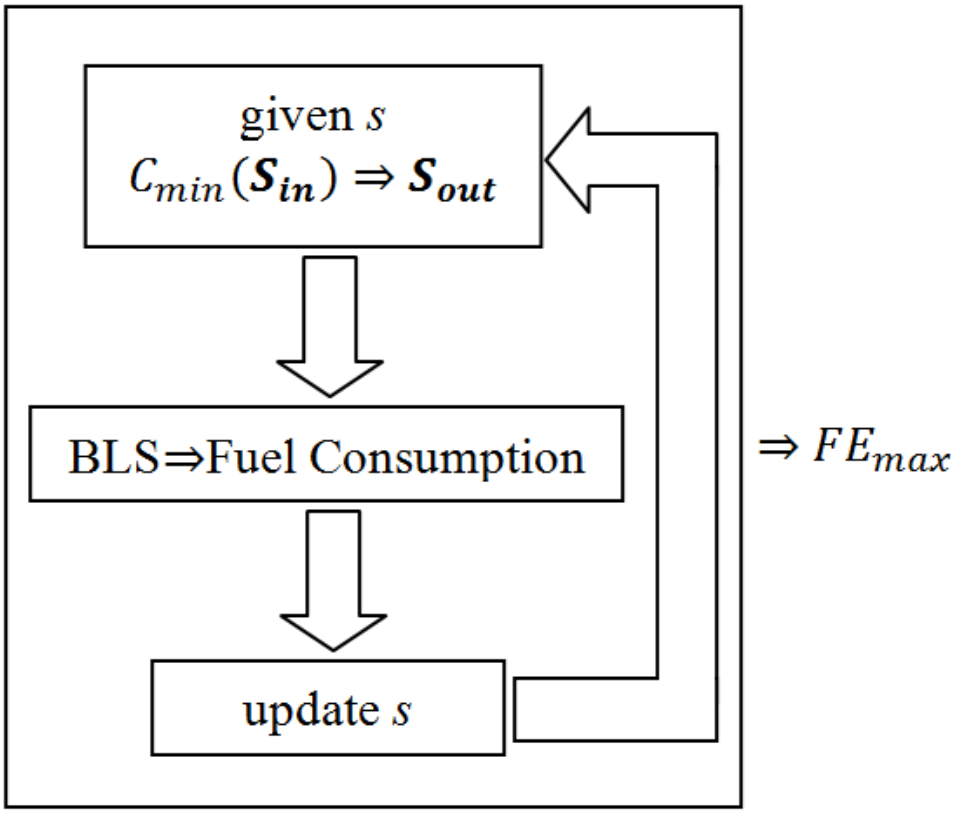

Figure 3.1: Two-term cost function supervisory control strategy design approach presented in Chapter 2

Although the described approach is useful for comparing and contrasting architectures, it does not easily translate to an implementable control strategy since 1) the two-term cost function does not penalize rapid transitions in IC engine speed, and 2) the steady-state model does not reveal detrimental transient behavior due to IC engine rotational inertia. This is consistent with other works which also neglect speed transients of various powertrain components and assume that engine speed can rise as fast as needed [36, 37]. The downside of the BLS two-term optimization is that it yields unrefined state transitions where IC engine speed varies rapidly in time, as evident in Figure 3.2. This

figure plots sample drive cycle simulation results from Chapter 2 for the THS-II system where rapid engine speed fluctuations exist. As previously noted, IC engines are best suited for constant speed operation. The IC engine state transitions shown in Figure 3.2 are not only difficult to achieve, but due to engine inertia, may also force actual powertrain operation to employ inferior output states while attempting to achieve the engine speed fluctuations. Problematic IC engine state transitions can also jeopardize consumer acceptability with unnecessary powertrain noise, vibration, and harshness (NVH). For these reasons, two methods will be investigated herein for *refining* IC engine state transitions: 1) smoothing the two-term optimization results, and 2) introducing a three-term cost function.

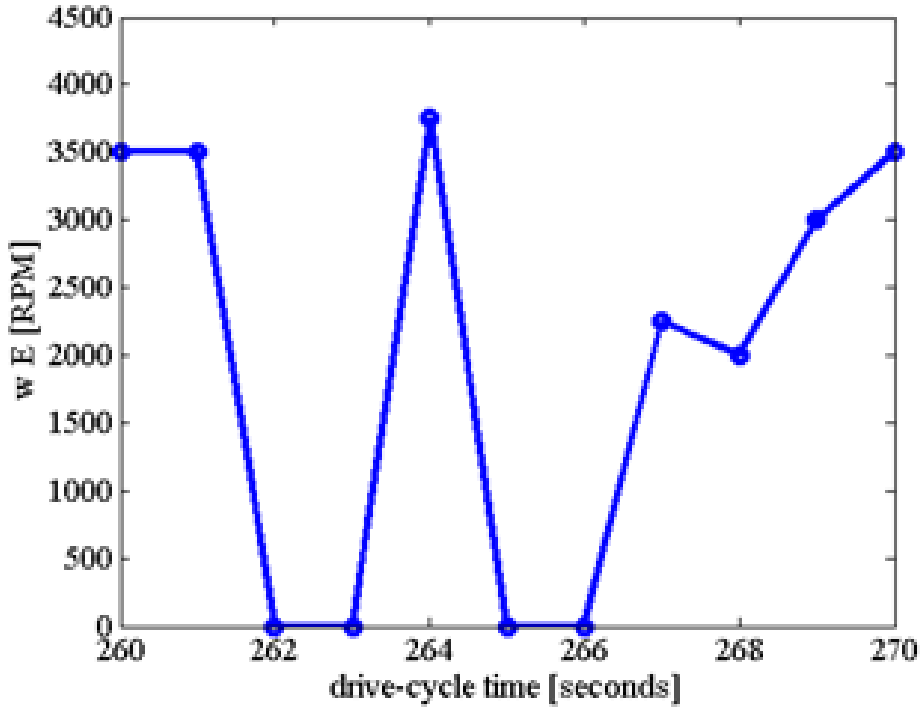

Figure 3.2: THS-II UDDS two-term cost function engine speed in BLS

3.1 Control Strategy Overview

An implementable supervisory control strategy, with refined engine speed transitions, is developed next using backward-looking and forward-looking simulations. Computationally-efficient BLS employs steady-state modeling equations and explicit following of a drive cycle to compute vehicle acceleration/deceleration and subsequent power required. It is not constrained by the need for a stable time step, is quick to compute, and is straight-forward to program. On the other hand, FLS calculations are carried out in a high-fidelity and forward time-marching fashion using equations of motion. A driver request is derived from a drive cycle and translated into the required energy output demanded of powertrain components (e.g., EMs, IC engine, and the high voltage battery). Importantly, transient behavior of components with non-negligible inertia is captured in a FLS model, and not in a BLS model. FLS captures transient motions using high-order integration schemes with relatively small variable time-steps to solve the following differential equations of motion for each component,

$$\sum F = m\frac{dV}{dt}, \tag{3.1}$$

$$\sum M = \frac{dH}{dt}. \tag{3.2}$$

In Equation (3.1) and Equation (3.2), F denotes the external force on the component, m its mass, V its velocity, M the resultant external moment, and H the angular momentum. These equations of motion are integrated to yield the vehicle's state from one time-step to the next.

Since BLS is modeled with steady-state equations, it can be used to produce results quickly and easily. More accurate FLS can then be used to verify and tune supervisory control strategies developed in BLS. FLS is particularly desirable for hardware development and detailed control strategy simulation (e.g., frequency analysis) but has slower execution times relative to BLS. For these reasons, this work suggests the two phase development process shown in Figure 3.3 to design implementable HEV supervisory control strategies.

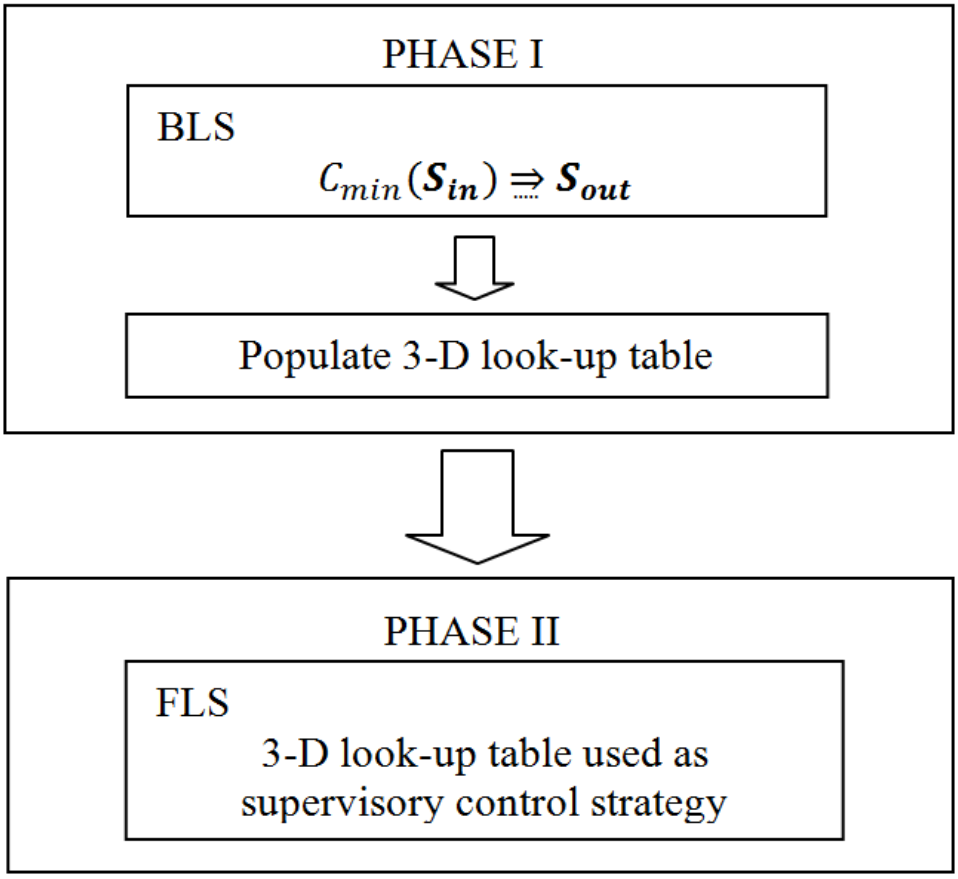

Figure 3.3: Two phase supervisory control strategy development process

In Phase I, all expected road-load conditions, kinematic constraints, and SOCs are used to populate a look-up table which given an input-state $\boldsymbol{S_{in}}$, returns an optimized output-state $\boldsymbol{S_{out}}$. In Phase I, the input-state $\boldsymbol{S_{in}}$ implies the output-state $\boldsymbol{S_{out}}$ through the instantaneous minimization of the cost function *C*. In Phase II, the generated look-up table is implemented as an open-loop control strategy in FLS. The three-dimensional data structure in Figure 3.4 can be used to store the control strategy where $\boldsymbol{S_{in}}$ is the table's input and $\boldsymbol{S_{out}}$ is the table's output. Note that to implement in FLS, each axis in Figure 3.4 is discretized into a finite number of values. In FLS high-order integration routines require stable time steps as small as nanoseconds (ns), which is an unnecessarily frequent sampling time for the control strategy. Thus for computational efficiency, control strategy output-states are sampled at a set frequency much lower than that of time stepping, and linear interpolation is used when necessary. The transient response of the steady-state Phase I control strategy is then studied in Phase II and any necessary refinements are carried-out.

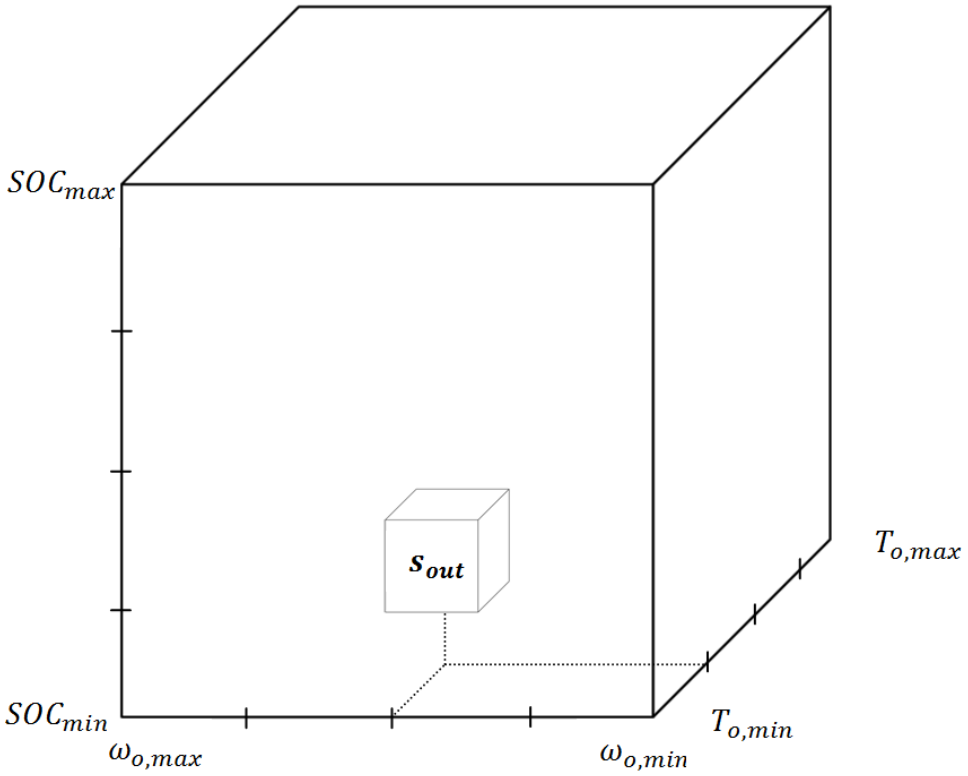

Figure 3.4: Three-dimensional structure storing pre-computed solutions

3.2 Forward-Looking Simulation Model

This section provides technical background on the operation of the Toyota THS-II architecture and its representation using backward and forward-looking simulation models. Note that all drive cycle simulations, whether backward-looking or forward-looking, are performed using the UDDS cycle [38]. The refinement of engine transients will be considered in the context of the THS-II system, but equally applies to refining the engine transients in the GM AHS-II system.

3.2.1 THS-II Forward-Looking Simulation

The highest level of the THS-II FLS is shown in Figure 3.5. The vehicle parameters used to define this model are found in [11]. Of the parameters not found in [11], common

values were assumed *i.e.*, EM inertia, IC engine inertia, etc. The driver model specifies a throttle position required to follow the user-defined drive-cycle and the controller stores the three-dimensional structure shown in Figure 3.4. The controller model routes required control signals to the plant's sub-models. As depicted, controller area network (CAN) signals enable communication between the three models and are named System_Signals in the FLS. The THS-II Simulink model used in this work is available at the second author's web page [39].

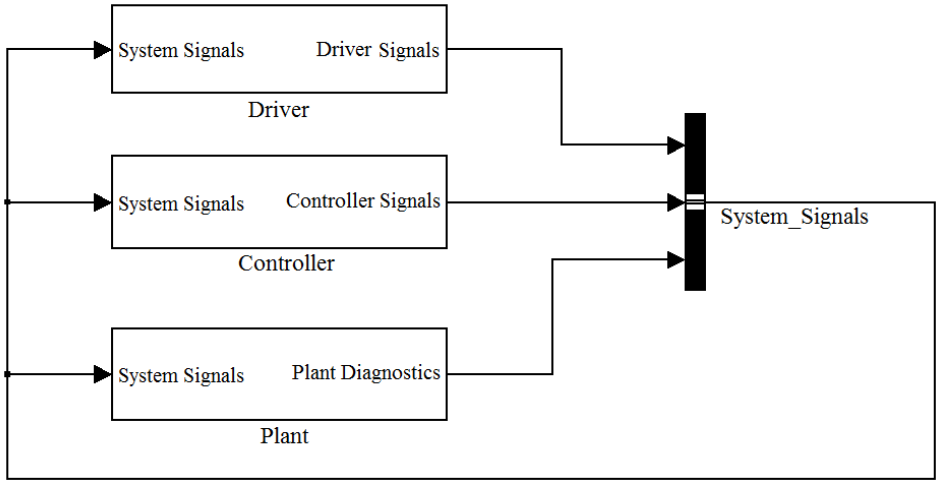

Figure 3.5: High-level THS-II FLS model

Mechanical connections within the powertrain are modeled using SimScape's SimDriveline axes with rotational inertias derived from the physical system. An overview of the Simulink THS-II power-plant model is shown in Figure 3.6. Depicted are component sub-models: battery, engine, *M/GA*, *M/GB*, and vehicle. The battery sub-model uses the EMs' current draw and updates SOC. The IC engine sub-model uses the output-state's engine speed and torque to determine the ensuring fuel consumption from

the engine's characteristic BSFC map. The two EMs are characterized by their efficiency surfaces within their respective sub-models.

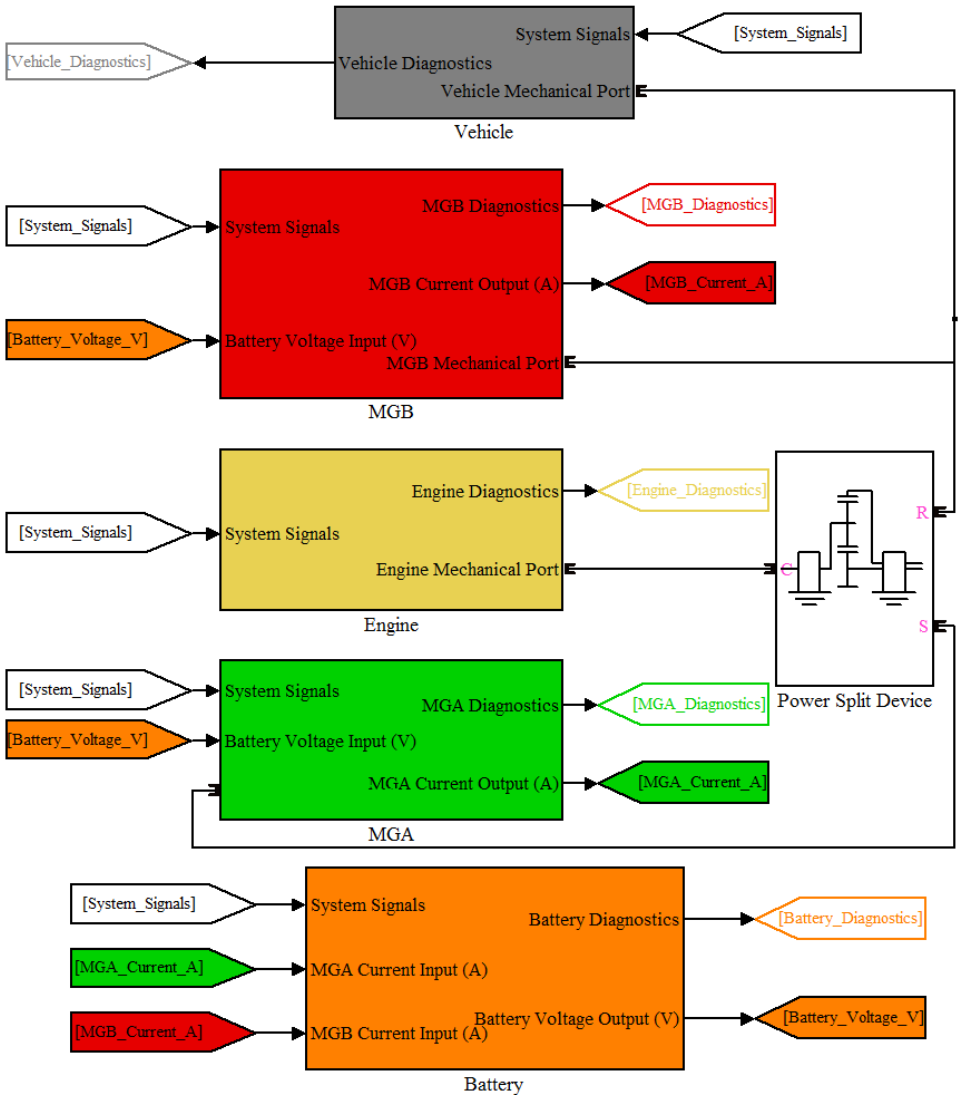

Figure 3.6: THS-II FLS plant showing component sub-models

The THS-II PSD is modeled as a standard Simulink Planetary Gear block with the THS-II characteristic ratio *R*. The IC engine is rigidly connected to the PSD carrier gear, *M/GA* drives the PSD sun gear, and *M/GB* contributes to the PSD ring gear tractive

effort. *M/GA* is controlled by a proportional-integral-derivative (PID) block to ensure it follows the engine speed dictated by $\boldsymbol{S_{out}}$. *M/GA* either consumes or regenerates electrical current to respectively accelerate or decelerate the IC engine as needed. The EM currents are routed to the battery, mimicking the high voltage bus of the THS-II.

The driver model used in the forward-looking simulator is shown in Figure 3.7. This figure depicts a PID controller block generating a torque request from the difference between actual and desired vehicle speed. The torque request, output speed, and SOC can be used to define $\boldsymbol{S_{in}}$ at each time step of the drive-cycle. $\boldsymbol{S_{in}}$ is then routed to the controller model and input into the look-up table supervisory control strategy as shown in Figure 3.8. Interpolation is used between pre-computed solutions to find $\boldsymbol{S_{out}}$ every 0.01 seconds. The look-up table output $\boldsymbol{S_{out}}$ is then routed to the respective powertrain components. Once all component operation has been specified by $\boldsymbol{S_{out}}$, energy delivery and consumption of each component in the THS-II architecture is known.

The powertrain's output energy is then delivered to the driven axle and/or ESS. The vehicle sub-model used to internally solve the equations of motion in Simulink is shown in Figure 3.9. It is derived from SimDriveline's Simple Gear, Tire, and Longitudinal Vehicle Dynamics blocks. As shown, the output of the transmission is delivered to the vehicle sub-model's mechanical port, to the rear differential, and then to the vehicle's driven wheels. Once the tractive effort is found, the model updates vehicle speed and component states from one time-step to the next. These calculations are iteratively repeated until the entire drive-cycle has been traversed. Use of the two-term cost

function results in FLS will be explored next, and problematic operation will be identified in order to motivate the proposed refinement approaches.

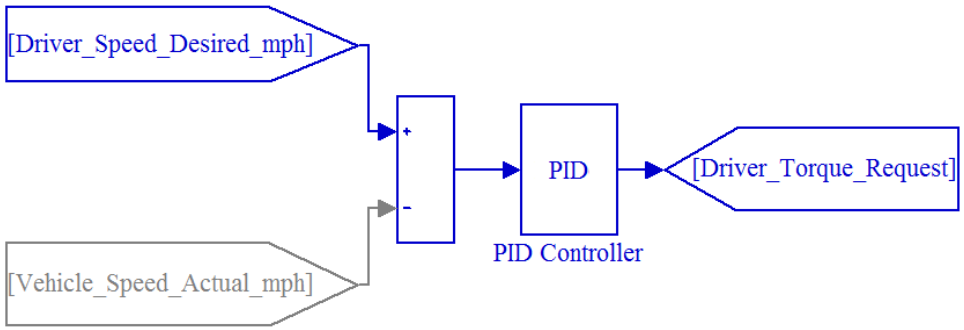

Figure 3.7: THS-II FLS driver model

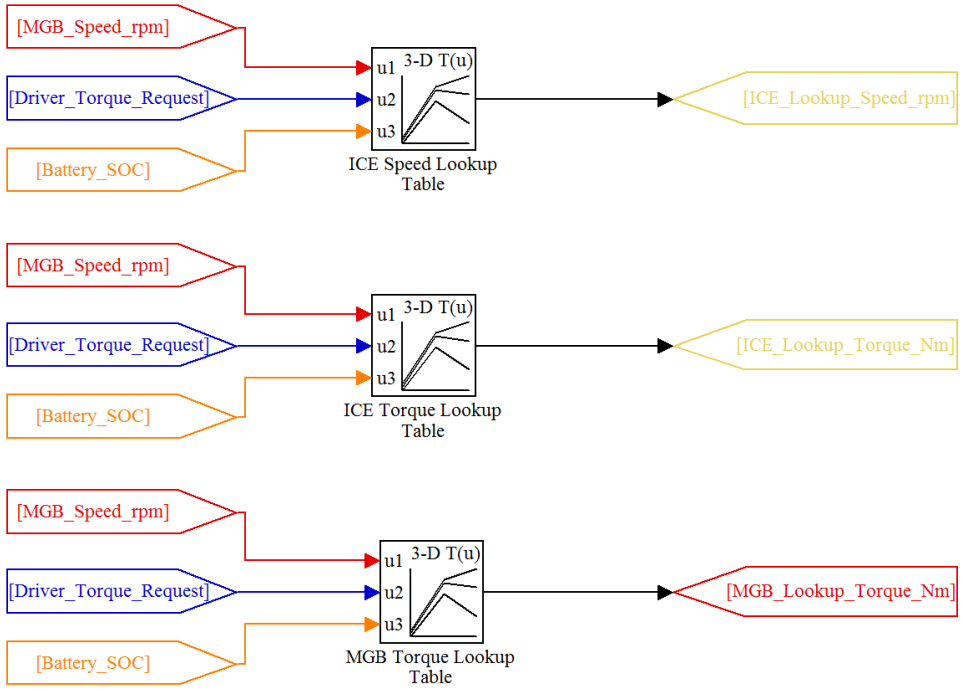

Figure 3.8: THS-II FLS supervisory controller model

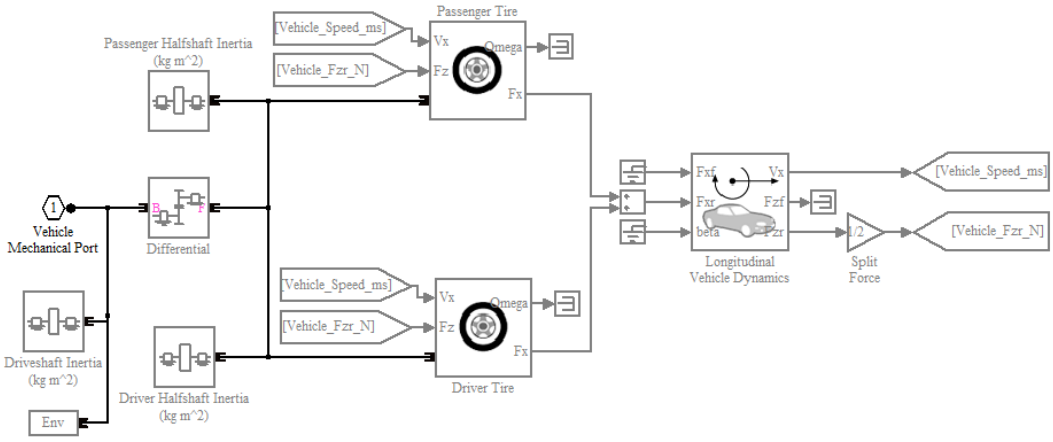

Figure 3.9: THS-II FLS vehicle sub-model

3.2.2 Unrefined Engine State Transitions in FLS

Of the information stored in $\boldsymbol{S_{out}}$, it can be reasonably assumed that $T_{M/GB}$ and T_e (through $\dot{m}_f$) can vary rapidly (or at least as quickly as the look-up table is sampled). On the contrary, ω_e is associated with engine inertia and cannot make large changes quickly. The unrefined transitions of the two-term optimization shown in Figure 3.2 are difficult and sometimes impossible to achieve due to the inertial resistance of the IC engine. This is evident in FLS results presented in Figure 3.10 where FLS-computed engine speeds are compared to that specified by the look-up table. The high frequency oscillations in engine speed resulting from the two-term optimization strategy are undesirable for efficient IC engine operation. Furthermore, they may not be achievable when engine inertia is accounted for, as it is in FLS. This is also evident in Figure 3.10 where a difference can be noted between FLS-calculated and look-up table-generated engine speeds. These differences are the result of finite *M/GA* power, making it impossible to achieve the engine transients specified by the look-up table. In summary, engine inertia

creates problematic state transitions and forces the powertrain to employ inferior states when *M/GA* cannot accelerate or decelerate engine speed as needed.

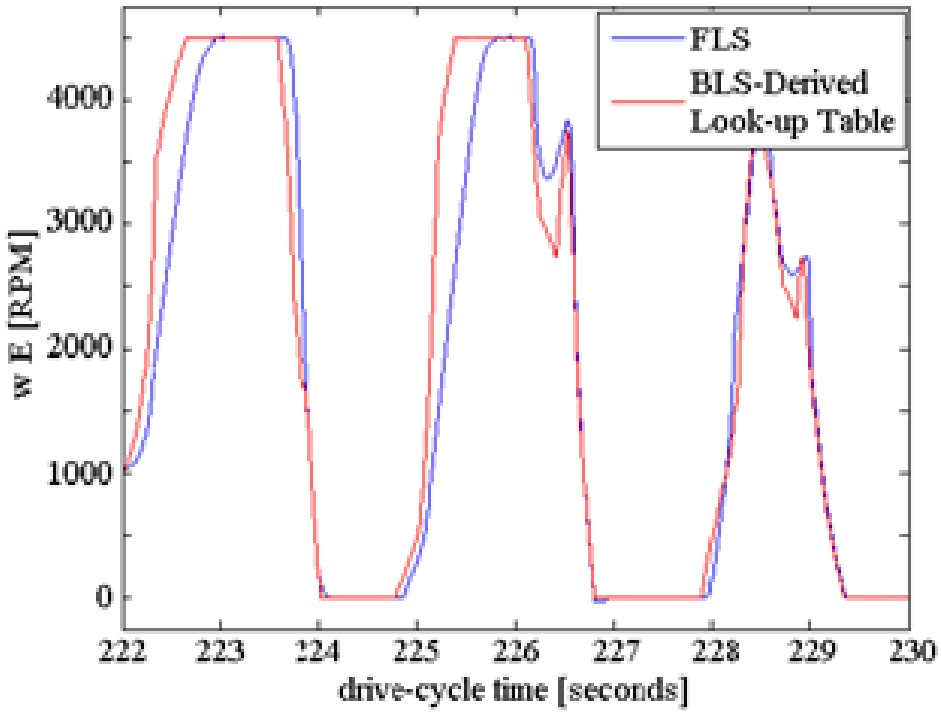

Figure 3.10: UDDS two-term cost function results in physics-based FLS

To investigate the cause of these state transitions, the three-dimensional look-up tables at constant SOC will now be inspected. Figure 3.11 shows examples of two-dimensional slices of the look-up table, at low-SOC and high-SOC, for all expected output torques and speeds. The *X*-axis denotes transmission output torque, the *Y*-axis transmission output speed, and the surface color represents IC engine speed. Note that EM torque curves exponentially decay as their rotational speed increases, as shown in Figure 3.12. Therefore maximum *M/GB* torque decreases as vehicle speed increases, explaining the rapid engine speed transitions in boxed region 1 of Figure 3.11. The surfaces also

contain scattered engine speed transitions, as marked in the second boxed region. These transitions can be attributed to large, concave changes in level sets of the engine's BSFC map. The constant SOC-slices also reveal the general operation of the engine resulting from the two-term cost optimization. On the low-SOC surface, the IC engine is predominately operated at the kinematically admissible upper limit to minimize charge depletion. As SOC builds, the necessity to regenerate charge, and thus dependence on the engine, decreases. As shown on the high-SOC surface, IC engine speed is set to the kinematically admissible lower limit to minimize charge regeneration.

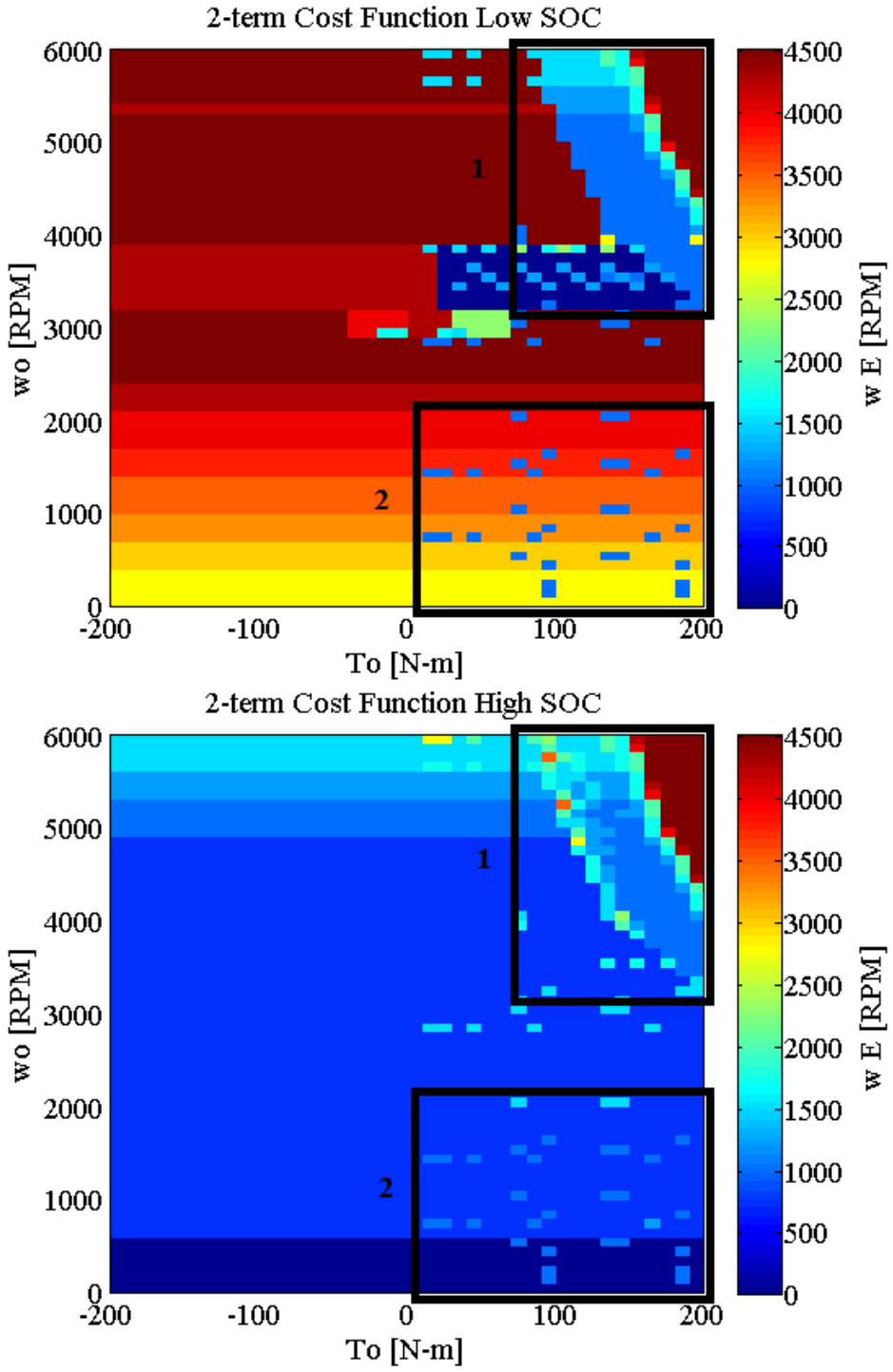

Figure 3.11: Two-term cost function IC engine speeds for expected road-load conditions, constant low-SOC and high-SOC

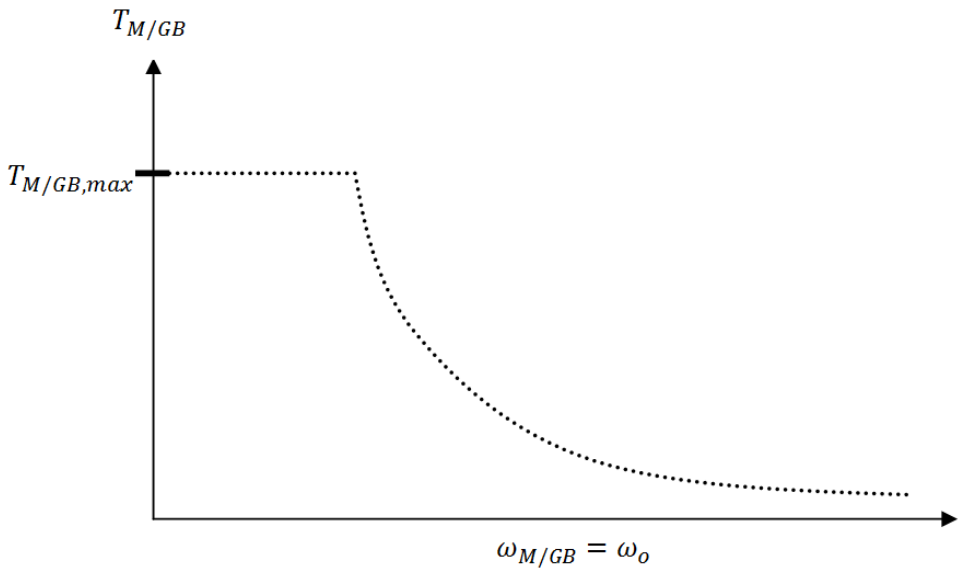

Figure 3.12: EM power curve

3.3 Results of Engine State Refinement Methods

Problematic IC engine state transitions motivate two methods for refining IC engine state transitions: i) smoothing the backward-looking two-term cost function results, and ii) introducing a three-term cost function penalizing changes in IC engine speed.

3.3.1 Smoothed Two-term Cost Function Results

The first refinement approach smooths engine speed transitions inside constant-SOC slices, such as those transitions observed in Figure 3.11. Multiple passes through each SOC slice are taken, varying the direction of smoothing from horizontal to vertical as shown in Figure 3.13. In the results to be initially presented, the maximum allowable engine speed change is $\Delta\omega_{max}$ = 1000 RPM and the smoothing increment is φ = 10 RPM. While scanning, if an engine speed transition is greater than $\Delta\omega_{max}$, the current

state's engine speed is adjusted by φ. If the current state's engine speed is faster than the next scanned state, the current state's engine speed is incremented by $-\varphi$. Similarly, if the current state's engine speed is slower than the next scanned state, the current state's engine speed is incremented by $+\varphi$. By repeatedly searching the constant SOC surfaces and applying $\pm\varphi$, the surfaces converge such that any state and its neighbors in all directions are within $\Delta\omega_{max}$.

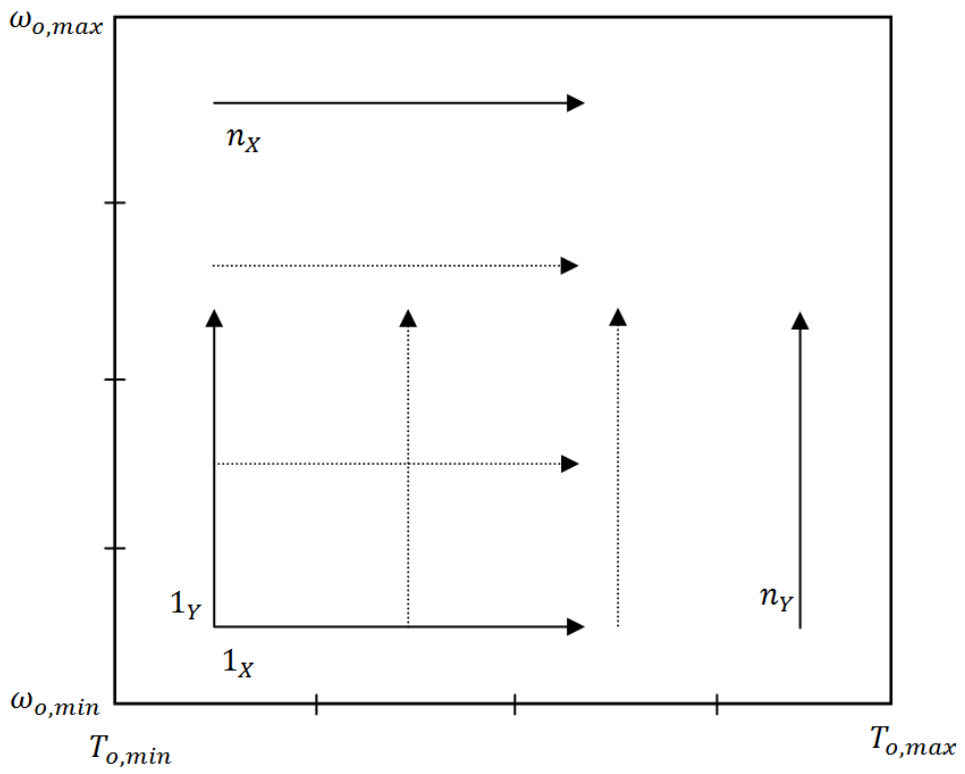

Figure 3.13: IC engine speed smoothing approach where n_X and n_Y are the nth iterations in the *X* and *Y*-dimensions respectively

Figure 3.14 presents the results of smoothed engine speed surfaces at low and high SOC. As desired, engine speed transitions are greatly improved. In particular, the undesirable

transitions in boxed region 1 of Figure 3.11 have been eliminated, and the sharp, localized transitions in boxed region 2 have been greatly reduced. Two issues arise in the smoothing approach however. First, depending on how the surfaces are smoothed, *i.e.*, the *X* or *Y*-direction first, different IC engine states are converged upon. Second, altering the original two-term cost function solution introduces inferior fuel consuming states relative to the original two-term cost function results.

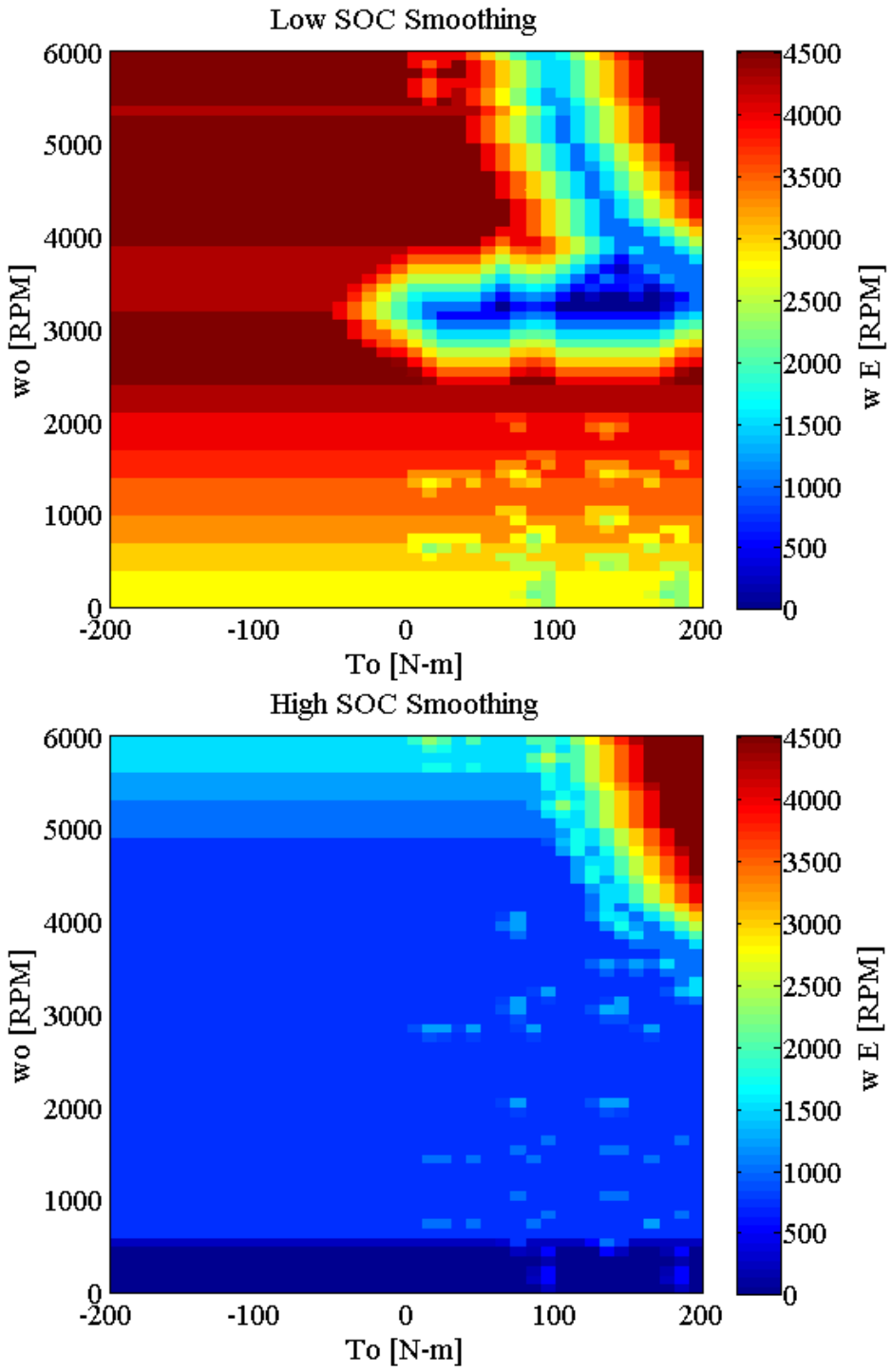

Figure 3.14: Smoothed two-term cost function IC engine speeds, constant low-SOC and high-SOC

3.3.2 Three-Term Cost Function

The second refinement approach employs a multi-objective cost function consisting of three terms: 1) fuel consumption, 2) battery power, and 3) change in IC engine rotational speed. The new three-term multi-objective cost function *C* is defined as,

$$C = P_f + sP_B + d, \tag{3.3}$$

where *d* is an additional cost of changing IC engine speed. The cost *d* is a function of the change in IC engine speed. An example profile for *d* is plotted in Figure 3.15. The figure shows that once engine speed changes more than $\Delta\omega_{max}$, the cost *d* dramatically increases. The added third term of the cost function prevents unrealistically accelerating and decelerating engine speed by heavily penalizing problematic IC engine state transitions.

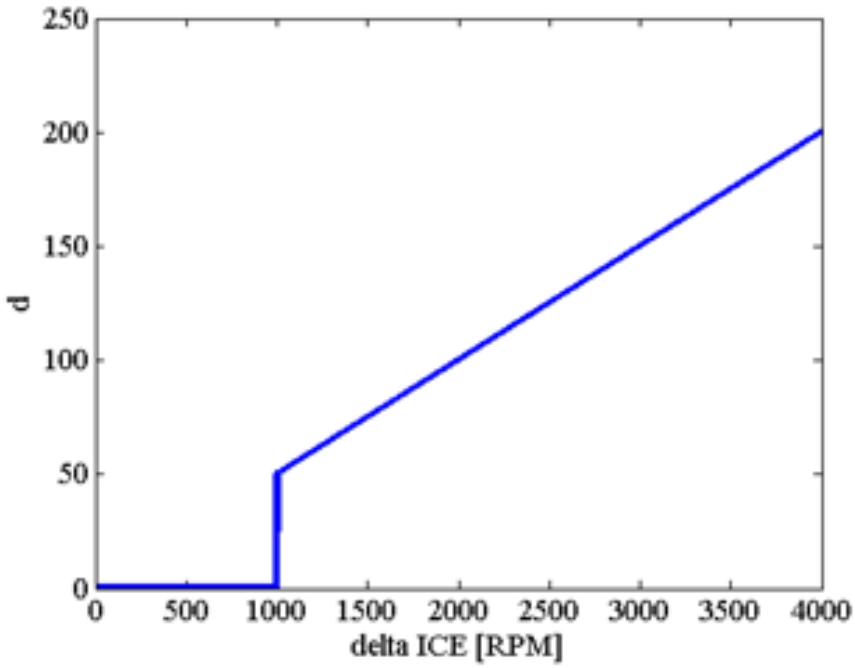

Figure 3.15: Cost of accelerating IC engine speed *d*

Figure 3.16 displays the three-term cost function design approach. Given *d* and *s*, BLS and the three-term cost function provide a fuel consumption estimate. As in the two-term cost function approach (depicted in Figure 3.1), different battery power management strategies and FE result from varying the form of the electric power equivalence factor *s*. Therefore for each *d*, the *s* resulting in maximized FE must be found as an inner optimization loop.

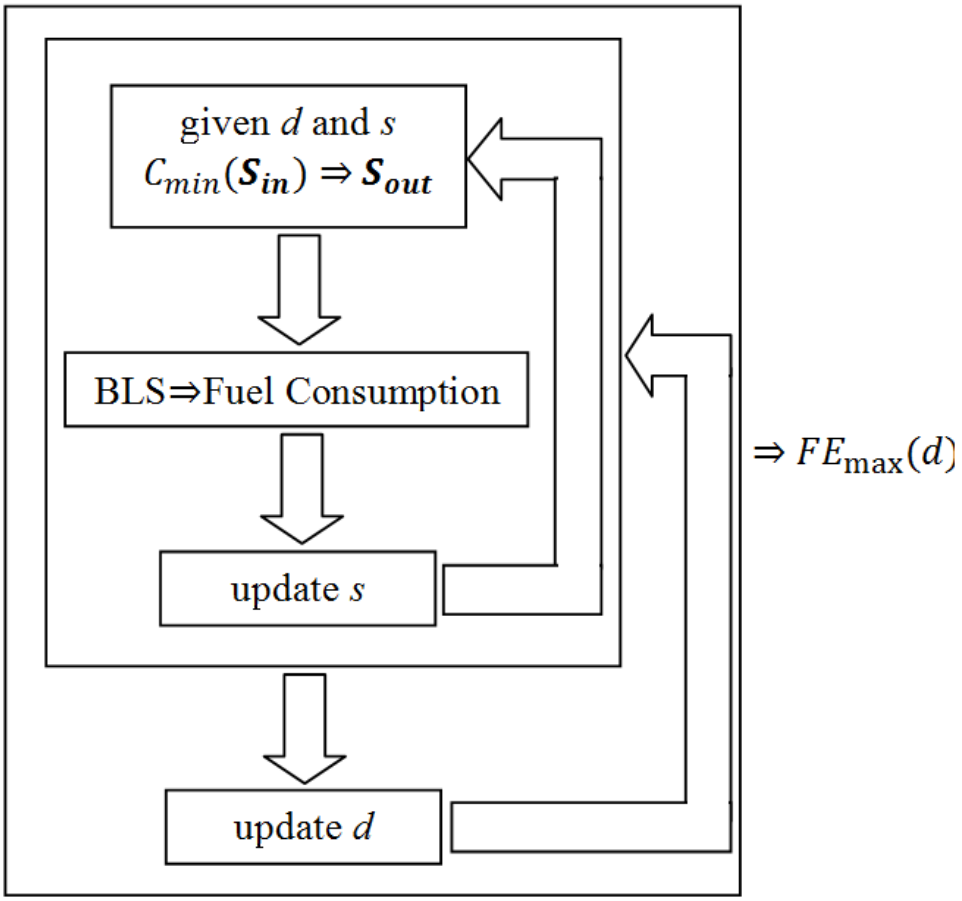

Figure 3.16: Three-term cost function supervisory control strategy design approach

Figure 3.17 provides an example IC engine speed time-history resulting from the three-term cost function BLS optimization. In comparison to Figure 3.2, the high frequency engine speed oscillations are eliminated by the three-term cost function, as desired.

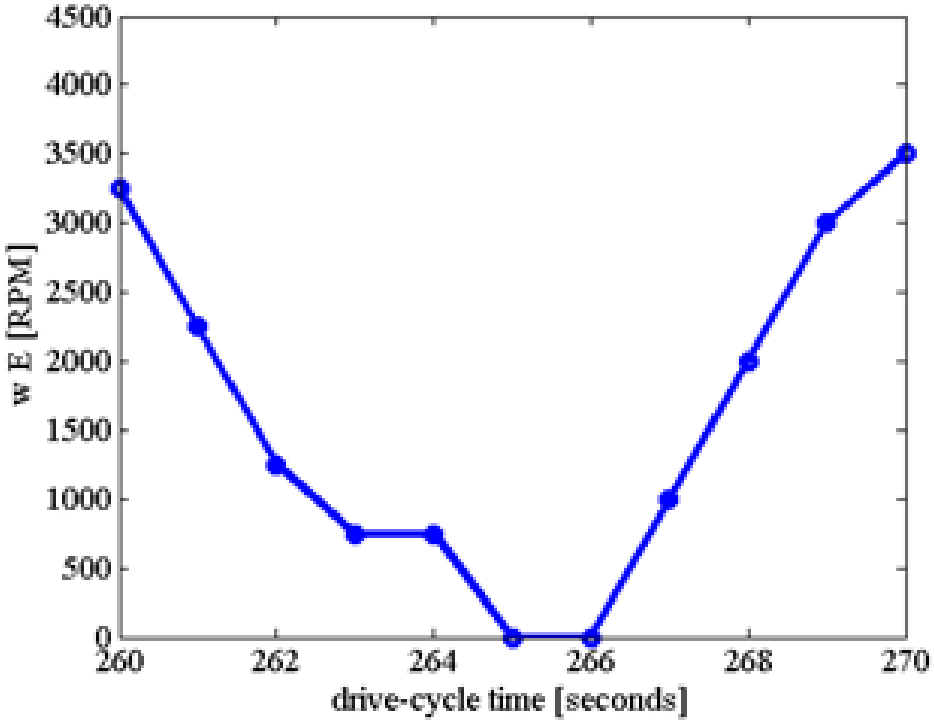

Figure 3.17: UDDS three-term cost function engine speed

With the strategy verified for $\Delta\omega_{max}$ = 1000 RPM, the effect on fuel economy of increasing $\Delta\omega_{max}$ is explored in Table 3.1. The table provides the BLS-computed FE estimates in MPG resulting from different selections for $\Delta\omega_{max}$. It also contains the FE estimate from the original two-term cost optimization and the two-term smoothing approach. The two-term cost function smoothing results introduce inferior FE states and significantly reduces FE. Note that the three-term $\Delta\omega_{max}$ = 4500 RPM optimization

selects the same output-states as the two-term cost function, verifying the implementation of the approach; however, in practice, 4500 RPM engine speed variations are unacceptable for the reasons discussed earlier.

Table 3.1: UDDS BLS fuel economy estimates

Optimization Method	BLS Fuel Economy (MPG)
2-term from Chapter 2	64.83
2-term smoothing	58.07
3-term, $\Delta\omega_{max}$ = 1000 RPM	62.92
3-term, $\Delta\omega_{max}$ = 1250 RPM	63.61
3-term, $\Delta\omega_{max}$ = 1500 RPM	64.53
3-term, $\Delta\omega_{max}$ = 4500 RPM	64.83

3.4 Results of Forward-Looking Simulation

Next the refinement approaches are implemented as control strategy look-up tables in forward-looking simulation, again using the UDDS drive cycle. This amounts to Phase II of the suggested control strategy development process. The results of Phase II are collected and presents in Table 3.2. This table displays the computed fuel economy and the percent time the simulated engine speed is within 5% of the look-up table engine speed. The latter metric is a strong indicator of the appropriateness of the steady-state assumption inherent in BLS, while both metrics taken together directly assesses the

quality of the BLS-derived control strategies. Note that all strategies closely follow the vehicle speed trace shown in Figure A.2 of Appendix A by delivering the road-load requirements.

Table 3.2 quantifies the trade-off between commanding ideal engine operating points (top row labeled '2-term') and being able to achieve them in FLS (other rows). The refinement methods were developed to reduce undesirable engine speed transients in the two-term cost function approach; therefore the two-term cost function results provide a baseline performance for comparison. Note from the third column of the table that the two-term strategy's FLS-computed engine speed deviates significantly from the BLS-derived engine speed. This results in inferior FE (61.65 MPG in FLS versus 64.83 MPG in BLS) since the engine must transition through poor BSFC efficiency regions while trying to achieve the BLS-derived control points (e.g., engine speed). The first refinement approach explored (smoothing of the two-term look-up table) is observed to significantly increase the percent time the FLS-computed engine speed is within 5% of the look-up table's commanded value, as desired, but achieves the lowest FE of any approach – it is even lower than the FE achieved by the unrefined two-term approach. The reason for this is that the smoothed two-term control strategy chooses less efficient, but more achievable, engine operating points.

The second refinement approach explored fares better than the first. The second column of Table 3.2 shows that 0.47% of the commanded engine speed transitions cannot be achieved for $\Delta\omega_{max}$ = 1000 RPM, 1.06% for $\Delta\omega_{max}$ = 1250 RPM, and 1.27% for $\Delta\omega_{max}$

= 1500 RPM. All of these numbers significantly improve upon the unrefined two-term approach and are acceptable for control strategy implementation. As engine speed is permitted to vary up to 1500 RPM, FE increases at the expense of slight decreases in following the BLS-derived engine speeds. Although not provided in the table, it is noted that as engine speed is permitted to vary by more than 1500 RPM, engine transient operation increases and FLS-computed engine speeds begin to fall off the BLS-derived engine speed trace more frequently, indicating an unachievable control strategy. The $\Delta\omega_{max}$ = 1500 RPM strategy is found in this study to be the best approach since it does not restrict engine speed too strictly, while at the same time not commanding unachievable states. The FLS-computed FE of this strategy is 64.10 MPG, which is very close to the estimate of 64.53 MPG computed by BLS. It is also noted that the FLS FE estimate for the $\Delta\omega_{max}$ = 1500 RPM strategy is 4% lower than the THS-II estimates presented in [31] using a time horizon dependent dynamic programming technique. Recall that DP techniques find optimal control strategies using global drive cycle information, and therefore provide a theoretical upper limit for fuel economy.

Table 3.2: UDDS FLS fuel economy estimates

Optimization Method	FLS Fuel Economy (MPG)	% operation engine speed within $\pm 5\%$ look-up
2-term	61.65	93.45
Smoothed 2-term	57.86	99.61
3-term, $\Delta\omega_{max}$ = 1000 RPM	62.61	99.53
3-term, $\Delta\omega_{max}$ = 1250 RPM	63.27	98.94
3-term, $\Delta\omega_{max}$ = 1500 RPM	64.10	98.72

The final discussion concerns the efficacy of efficient, but approximate backward-looking simulations and their justification for use in a two-phased control strategy development process. The central idea is that if, after all design iterations have been completed in the design process (see Figures 3.3 and 3.16), component time-history traces dictated by the BLS-derived and refined look-up table match those actually achieved in FLS, then the use of BLS in determining the look-up table is warranted. Note that without the use of BLS, development and optimization of the supervisory control strategy is significantly more difficult and vastly more time consuming. Figure 3.18 displays engine speed and *M/GA* electrical power time-history traces comparing BLS-commanded component operation with FLS-computed response using the $\Delta\omega_{max}$ = 1500 RPM strategy. The top sub-figure shows very clearly that the FLS-computed and look-up

table commanded engine speeds are in close agreement. The bottom sub-figure shows that when the engine speed is close to steady, the FLS-computed *M/GA* electrical power deviates little from the look-up table commanded power. However, when the engine speed must be accelerated or decelerated to achieve a more desirable state, the *M/GA* electrical power can have short-lived sharp spikes that deviate from the look-up table *M/GA* electrical power. This is to be expected, however, since a primary role of *M/GA* is to accelerate/decelerate the IC engine so that it quickly and efficiently reaches its desired operating point. Furthermore, these *M/GA* power spikes are limited in duration and carry a much lower efficiency penalty than similar spikes in engine operation. In summary then, the overall close comparison of the BLS and FLS results in Figure 3.18 justify the use of BLS-derived and optimized look-up tables in the two-phase design process.

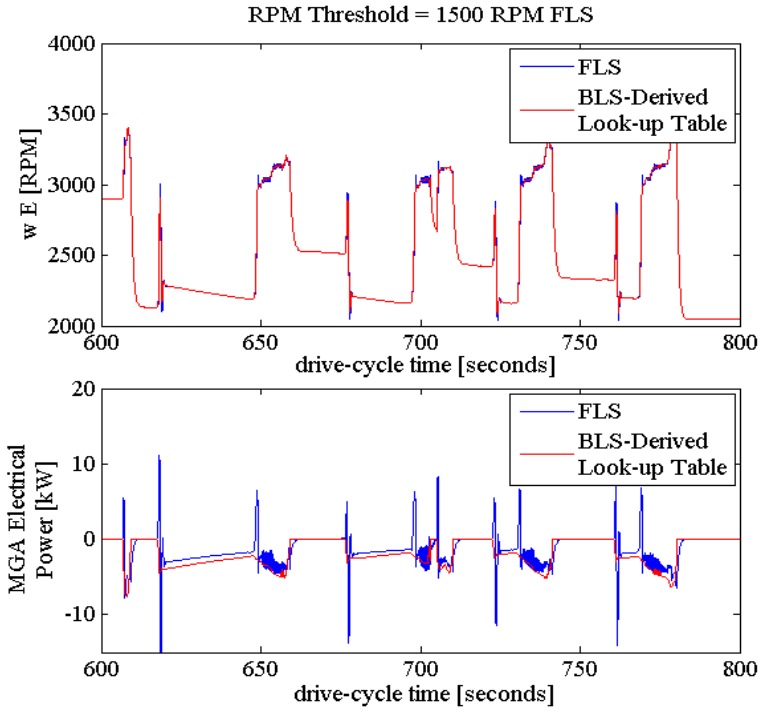

Figure 3.18: UDDS RPM Threshold = 1500 RPM FLS results

CHAPTER 4

CONCLUDING REMARKS

In summary, Chapter 2 of this work uses a two-term cost function in conjunction with steady-state backward-looking simulation to find supervisory control strategies resulting in minimized fuel consumption for two different studied powertrains. This cost function exhaustively searches all admissible operating states and determines the power split between internal combustion engine and stored on-board electric energy. The two-term cost function results in unacceptable engine speed transitions because steady-state backward-looking simulations do not consider internal combustion engine inertial resistance. Although this method provides quick, computationally inexpensive fuel economy estimates, speed and energy transients are neglected. In physics-based forward-looking simulations, the fuel minimizing two-term cost function internal combustion engine state transitions are difficult to achieve. When not achieved, the optimizations' results are employed in a non-desirable manner. To address this deficiency, two refinement techniques have been explored together with the introduction of a two-phase control strategy development process utilizing backward-looking and forward-looking simulations. The refinement methods detailed include: 1) smoothing the two-term optimization look-up table results, and 2) introducing a three-term cost function. These refinement methods were tested and verified in forward-looking simulations.

It is found through forward-looking simulations that both refinement methods achieve operable engine speed transitions, and result in fuel economy estimates which compare

well to back-ward looking simulation results. Furthermore, it is found that the three-term cost function finds more efficient operating points than the smoothed two-term cost function approach, and that the predicted fuel economy is close to the optimal dynamic programming fuel economy published in the literature. Close comparisons are documented for component operation dictated by the BLS-derived control strategy with that computed using FLS. This justifies the efficacy of the two-phased design process of generating look-up tables using BLS, and computing transient component operation and final fuel economy measures in FLS. Therefore, this process is suggested for rapid and effective development of HEV supervisory control strategies in future work.

APPENDIX A

A.1 Unified drive-cycle

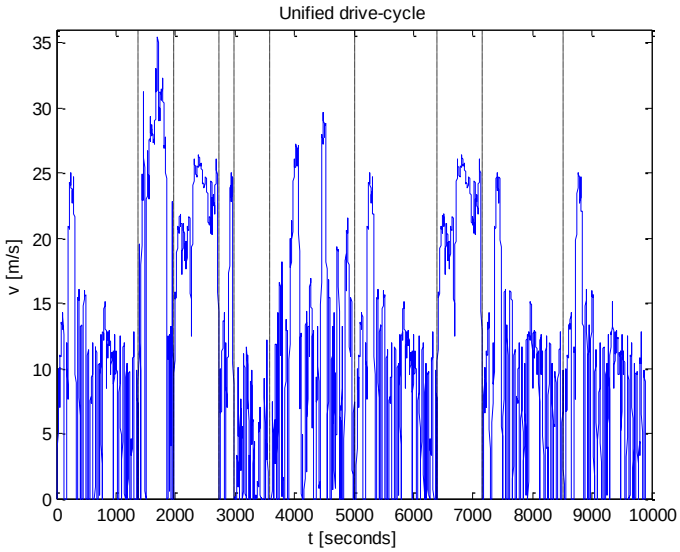

Figure A.1: Combined urban-rural unified drive-cycle

A.2 UDDS drive-cycle

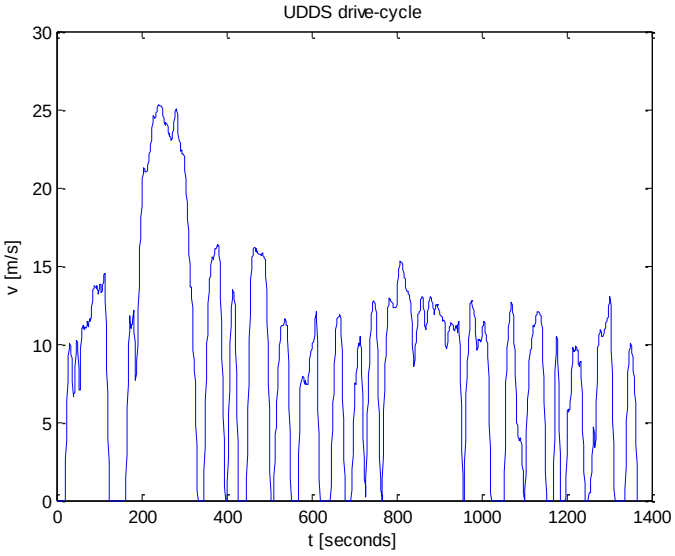

Figure A.2: UDDS drive-cycle [37]

REFERENCES

[1] U.S. Energy Information Administration, "Petroleum & Other Liquids," http://www.eia.gov/dnav/pet/hist/LeafHandler.ashx?n=PET&s=WTOTUSA&f=W, June 2011.

[2] National Highway Traffic Safety Administration, "CAFÉ Overview – Frequently Asked Questions," http://www.nhtsa.gov/cars/rules/cafe/overview.htm, June 2011.

[3] Vlasic, B., New York Times, "Obama Reveals Details of Gas Mileage Rules," http://www.nytimes.com/2011/07/30/business/energy-environment/obama-reveals-details-of-gas-mileage-rules.html?_r=1, July 2009.

[4] United States Environmental Protection Agency, "Regulations and Standards," http://www.epa.gov/fueleconomy/regulations.htm, June 2011.

[5] United States Environmental Protection Agency, "Our Mission and What We Do," http://www.epa.gov/aboutepa/whatwedo.html, June 2011.

[6] United States Environmental Protection Agency, "Cleaner Passenger Vehicles & Gasoline, Clean Cars + Clean Fuel = Cleaner Air," http://www.epa.gov/tier2/, June 2011.

[7] Merriam-Webster, http://www.merriam-webster.com/dictionary/hybrid, June 2011.

[8] EV World, THE FUTURE IN MOTION, "TOYOTA HYBRID SYSTEM THIS-II," http://www.evworld.com/library/toyotahs2.pdf, June 2011.

[9] Gelb, G., Richardson, N., Wang, T., and Berman, B., "An Electromechanical Transmission for Hybrid Vehicle Powertrains," SAE paper no. 710235, 1971.

[10] Miller, J., "Comparative assessment of hybrid vehicle power split transmissions," Fourth VI Winter Workshop Series, 2005.

[11] Olszewski, M, "Evaluation of 2004 Toyota Prius Hybrid Electric Drive System," Oak Ridge National Laboratory Report FY2006, pg. 1-95, 2006.

[12] Meisel, J., "An analytic foundation for the Toyota Prius THS-II powertrain with a comparison to a strong parallel hybrid-electric powertrain," SAE paper 2006-01-0666, 2006.

[13] Ahn, K., Cho, S., Lim, W., Park, Y., Lee, J.M., "Performance analysis and parametric design for the dual-mode planetary gear hybrid powertrain," *Proceedings of the Institution of Mechanical Engineers, Part D: Journal of Automobile Engineering*, 2006, 220(10), pg. 1601-1614.

[14] Conlon, B., "Comparative Analysis of Single and Combined Hybrid Electrically Variable Transmission Operating Modes," SAE paper no. 2005-01-1162, 2005.

[15] Grewe, T., Conlon, B., and Holmes, A., "Defining the General Motors 2-Mode Hybrid Transmission," SAE paper no. 2007-01-0273, 2007.

[16] Meisel, J., "An analytic foundation for the two-mode hybrid-electric powertrain with a comparison to the single-mode Toyota Prius THS-II powertrain," SAE paper no. 2009-01-1321, 2009.

[17] Cho, S., Ahn, K., and Lee, J., "Efficiency of the planetary gear hybrid powertrain," *Proceedings of the Institution of Mechanical Engineers, Part D: Journal of Automobile Engineering*, 2006, 220(10), pg. 1445-1454.

[18] Ahn, K., Cho, S., Cha, S., and Lee, J., "Engine operation for the planetary gear hybrid powertrain," *Proceedings of the Institution of Mechanical Engineers, Part D: Journal of Automobile Engineering*, 2006, 220(10), pg. 1727-1735.

[19] Ahn, K., Papalambros, P.Y., "Engine optimal operation lines for power-split hybrid electric vehicles," *Proceedings of the Institution of Mechanical Engineers, Part D: Journal of Automobile Engineering*, 2009, 223(9), pg. 1149-1162.

[20] Lin, C., Filipi, Z., Wang, Y., Louca, L., Peng, H., Assanis, D., Stein, J., "Integrated, Feed-forward Hybrid Electric Vehicle Simulation in SIMULINK and its Use for Power Management Studies," *SAE Paper* 2001-01-1334, 2001.

[21] Lin, C., Peng, H., Grizzle, J. W., Liu, J., and Busdiecker, M., "Control System Development for an Advanced-Technology Medium-Duty Hybrid Electric Truck," *SAE Paper* 2001-01-3369, 2003.

[22] Lin, C., Peng, H., Grizzle, J. W., Kang, J., "Power Management Strategy for a Parallel Hybrid Electric Truck," *IEEE Transactions on Control Systems Technology*, Vol. 11, pp. 839-849.

[23] Kim, N., Cha, S., Peng, H., "Optimal Control of Hybrid Electric Vehicles Based on Pontryagin's Minimum Principle," *IEEE Transactions on Control Systems Technology*, August 2010.

[24] Cipollone, R., Sciarretta, A., "Analysis of the Potential Performance of a Combined Hybrid Vehicle with Optimal Supervisory Control," *Proceedings of the IEEE International Conference on Control Applications*, pp. 2802-2807, 2006.

[25] Ahn, K., Cho, S., Cha, S., "Optimal Operation of the Power-split Hybrid Electric Vehicle Powertrain," *Proceedings of the Institution of Mechanical Engineers Part D: Journal of Automobile Engineering*, 225(5), pp. 789-800, 2008.

[26] Lin, C., Peng, H., Grizzle, J. W., "A Stochastic Control Strategy for Hybrid Electric Vehicles'," *Proceedings of the American Control Conference*, Boston, Massachusetts, 2004.

[27] Lin, C., "Modeling and Control Strategy Development for Hybrid Vehicles," *Dissertation*, University of Michigan, 2004.

[28] Piccolo, A., Ippolito, L., Galdi, V., Vaccaro, A., "Optimization of Energy Flow Management in Hybrid Electric Vehicles via Genetic Algorithms," *Proceedings of 2001 IEEE/ASME International Conference on Advanced Intelligent Mechatronics*, Como, Italy, 2001.

[29] Schouten, N., Salman, M., Kheir, N., (2002), "Fuzzy Logic Control for Parallel Hybrid Vehicles," *IEEE Transactions on Control Systems Technology*, Vol. 10, No. 3, pp. 460-468.

[30] Arata J., Leamy M., Meisel, J. Cunefare, K., Taylor, D., "Backward-Looking Simulation of the Toyota Prius and General Motors Two-Mode Power-Split HEV Powertrains," *SAE International Journal of Engines*, Vol. 120, June 2011.

[31] Liu, J., Peng, H., "Modeling and Control of a Power-Split Hybrid Vehicle," *IEEE Transactions on Control Systems Technology*, Vol. 16, No. 6, November 2008, pp. 1242-1251.

[32] Roos, F. and Spiegelberg, C., "Relation Between Size and Gear Ratio in Spur and Planetary Gear Trains," Royal Institute of Technology Technical report, 2004, http://www.md.kth.se/~fredikr/AM2S/gearReport.pdf.

[33] Litvin, F., Fuentes, A., Vecchiatto, D., Gonzales-Perez, I., "New design and improvement of planetary gear trains," Project report to NASA, University of Illinois at Chicago, 2004.

[34] General Motors, '1.6L Fam 1 for Teams.xls', EcoCAR resource, 2008.

[35] United States Environmental Protection Agency, "Dynamometer Driver's Aid," http://www.epa.gov/nvfel/testing/dynamometer.htm, July 2011.

[36] Serrai, L., Onori, S., Rizzoni, G., "A Comparative Analysis of Energy Management Strategies for Hybrid-Electric Vehicles," *Journal of Dynamic Systems, Measurements, and Control*, Vol. 133, May 2011, 031012-1.

[37] Li, C., Peng, H., "Optimal Configuration Design for Hydraulic Split Hybrid Vehicles," *2010 American Control Conference*, June 30-July 02, 2010, pp. 5812-5817, 978-1-4244-7427.

[38] Georgia Institute of Technology School of Mechanical Engineering, Nonlinear Mechanics Lab, http://www.me.gatech.edu/nlmechanics, June 2011.

[39] United States Environmental Protection Agency, "EPA Urban Dynamometer Driving Schedule UDDS," http://www.epa.gov/oms/standards/light-duty/udds.htm, June 2011.